



# Design and performance considerations for dual-sided microstructured semiconductor neutron detectors

T.R. Ochs<sup>a,\*</sup>, R.G. Fronk<sup>a,1</sup>, S.L. Bellinger<sup>b</sup>, D.S. McGregor<sup>a</sup>

<sup>a</sup> Semiconductor Materials and Radiological Technologies Laboratory, Department of Mechanical and Nuclear Engineering, Kansas State University, Manhattan, KS 66506, USA

<sup>b</sup> Radiation Detection Technologies, Inc., Manhattan, KS 66502, USA

## ARTICLE INFO

### Keywords:

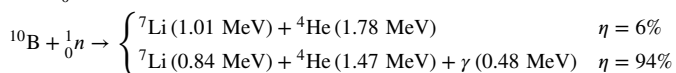
Neutron detector  
Microstructured semiconductor neutron detector  
Solid-state radiation detector  
Helium-3 replacement  
Dual-sided microstructured semiconductor neutron detector

## ABSTRACT

Thin-film-coated solid-state thermal neutron detectors were replaced in recent decades with the Microstructured Semiconductor Neutron Detector (MSND) technology. The basic device structure of the MSND involves micro-sized trenches that are etched into a vertically-oriented *pvn*-junction diode that are backfilled with a neutron converting material. Neutrons absorbed within the converting material induce fission of the parent nucleus, producing a pair of energetic charged-particle reaction products that can be counted by the diode. The deep-etched microstructures of the MSND yield good neutron-absorption efficiency and reaction-product counting efficiency, resulting in a 6-10x improvement in intrinsic thermal-neutron detection efficiency over thin-film-coated devices. Performance of present-day MSNDs are reaching an efficiency plateau; streaming paths between the conversion-material backfilled trenches, allow a considerable fraction of neutrons to pass through the device undetected. Dual-Sided Microstructured Semiconductor Neutron Detectors (DS-MSNDs) have been developed that utilize a complementary second set of trenches on the back-side of the device to capture streaming neutrons. This work investigates several of the fundamental design structures that can be etched into the semiconductor material, including repeated front-side and back-side patterns and inverse microfeature patterns. Results from MCNP6 simulations of DS-MSNDs show that intrinsic thermal-neutron detection efficiencies are often double that of their MSND counterparts and greater than 80% intrinsic thermal-neutron detection efficiency is theoretically possible with a 1.5-mm thick device.

## 1. Introduction

Recent investigations into replacements for <sup>3</sup>He-gas filled neutron counters have been centered on small-volume, low-cost, low-power, thermal-neutron sensors. One such early candidate for replacing the <sup>3</sup>He detectors included thin-film-coated semiconductor diodes wherein a thin film of neutron converting material, such as <sup>10</sup>B or <sup>6</sup>LiF, is coated over the leading surface of the device [1–4]. The thin-film-coated diodes detect charged-particle reaction products produced from neutron capture within the film that interact within the semiconductor detector depletion region. A thermal neutron absorbed within either the <sup>10</sup>B or <sup>6</sup>LiF neutron-reactive film will induce fission of the parent nucleus and produce charged-particle reaction products,



where  $\eta$  represents the branching ratio of the reaction. The reaction products are emitted in opposite directions from the point of neutron

absorption and impart energy into the medium through which they travel via Coulombic-force interactions.

Reaction products that exit the conversion material into the semiconductor substrate can deposit energy into the detector depletion region, and electron–hole pairs excited by these interactions can be drifted across the device by an applied bias. The resulting current can then be amplified, measured, and recorded by counting electronics. However, self-absorption and solid-angle limitations on the reaction product trajectories and low neutron absorption efficiency of the thin reactive coatings limit the intrinsic thermal-neutron detection efficiency of these devices to only 4%–5% for both <sup>10</sup>B and <sup>6</sup>LiF films [5,6]. <sup>10</sup>B is a commonly used converter material due to its relatively-high thermal neutron absorption cross-section ( $\sigma_{th} = 3800 \text{ b}$ ). However, the low-energy reaction products can make separation of the neutron-induced signal from background noise challenging. <sup>6</sup>LiF has a lower absorption cross-section ( $\sigma_{th} = 940 \text{ b}$ ), but produces higher-energy reaction products, allowing for higher lower-level discriminator values and, therefore, greater gamma-ray discrimination.

\* Corresponding author.

E-mail address: [trochs@ksu.edu](mailto:trochs@ksu.edu) (T.R. Ochs).

<sup>1</sup> Present address: Idaho National Laboratory, Idaho Falls, ID 83402, USA.

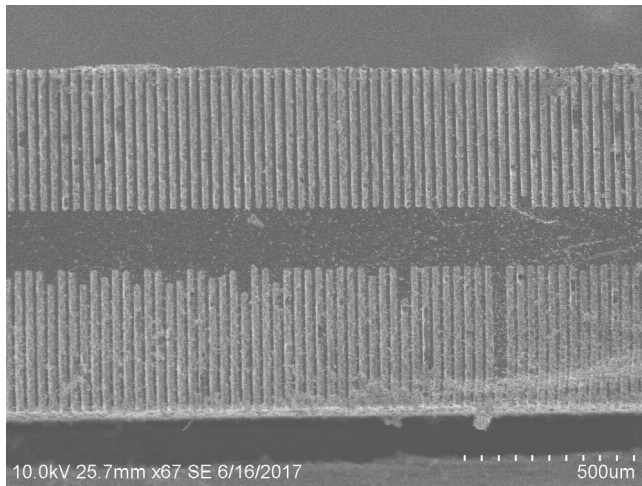


Fig. 1. Shown is an offset straight-trench DS-MSND design wherein two layers of trenches complement each other to produce an ultra-high efficiency neutron sensor.

It was suggested that microstructures could be formed into the semiconductor substrate and backfilled with neutron converting material to increase the intrinsic thermal-neutron detection efficiency [7, 8]. High-aspect ratio, deep-etched microcavities filled with neutron-sensitive material increases the intrinsic thermal-neutron absorption efficiency and increases the likelihood that charged-particle reaction products would escape the neutron-sensitive material region and be counted. The first prototype microstructured semiconductor neutron detectors (MSNDs) produced comprised a GaAs-based Schottky diode etched with micro-sized holes and backfilled with  $^{10}\text{B}$  powder [9]. More recent MSNDs feature straight-trench patterns etched as deep as 495  $\mu\text{m}$  and backfilled with nano-sized  $^6\text{LiF}$  powder [10]. Such devices have realized nearly a 10x increase in the intrinsic thermal-neutron detection efficiency over thin-film-coated diodes, with present-day MSNDs exceeding 30% intrinsic thermal-neutron detection efficiency for a 0.5-mm thick sensor and an active area of 1  $\text{cm}^2$  or 4  $\text{cm}^2$  [10–14]. However, MSNDs have reached an intrinsic thermal-neutron detection efficiency plateau for readily manufacturable microcavity geometries. Careful design of the trenches and semiconductor fins can optimize detection efficiency, but the semiconductor fins act as a neutron free-streaming path and force an upper theoretical limit on intrinsic thermal-neutron detection efficiency of approximately 45% for a single-sided MSND [11]. Many semiconductor substrates have small neutron-interaction cross-sections (for Si,  $\sigma_{\text{Si}} \approx 0.17$  b), thus neutrons normally-incident on the semiconductor substrate will likely pass undetected through the sensor [11]. To mitigate neutron free streaming, two MSNDs with 21% intrinsic thermal-neutron detection efficiency were double-stacked, aligned, and integrated to count as a single sensor yielding 42% detection efficiency [15,16]. However, proper alignment of the MSNDs was challenging and imprecise, which is not conducive to low-cost mass production.

To produce a sensor with detection efficiencies comparable to  $^3\text{He}$  detectors while also achieving low-cost mass-productibility, a new iteration of the perforated semiconductor diodes is needed and presented here. Dual-sided microstructured semiconductor neutron detectors (DS-MSNDs) have perforations etched into both sides of a semiconductor diode that are backfilled with neutron converting material (see Fig. 1) [17–20]. There are two basic types of DS-MSNDs; the offset-pattern design wherein front- and back-side patterns are staggered by half of a unit cell and repeated (similar to a stacked device), and an opaque-pattern design wherein front- and back-side patterns are an ‘inverse’ image of one another. The offset feature design is simpler to fabricate but streaming paths can still exist if the backfilled-microcavity critical dimension is too small, and front-side microcavities

may shadow back-side microcavities if the microcavity dimension is large. The opaque design allows for good neutron converter coverage even with complicated hole-type or pillar-type patterns. Presented here are theoretical considerations for intrinsic thermal-neutron detection efficiency for numerous microstructures with varying dimension.

## 2. Computational considerations

Monte Carlo simulations have previously determined the theoretical performance of single-sided MSNDs [11]. Intrinsic thermal-neutron detection efficiency was determined for semiconductor diodes as a function of neutron conversion material, perforation dimensions, and perforation depths for circular holes, circular pillars, and straight trenches. The present work is an extension of previous work [11], but now using MCNP6.1 to determine similar performance characteristics for DS-MSNDs, of similar dimensions and microstructure geometry. Cases for straight trenches, circular holes, and circular pillars will be considered. For each pattern, offset and opaque pattern types will be considered and backfilled with  $^{10}\text{B}$  or  $^6\text{LiF}$ . The overall device thickness will be limited to 500  $\mu\text{m}$  and 1500  $\mu\text{m}$  for  $^{10}\text{B}$ -based and  $^6\text{LiF}$ -based detectors, respectively.

For each design, the perforations are assumed to be backfilled with neutron conversion material powder with a packing fraction of 0.5. The packing fraction is defined as the ratio of the density of the conversion material powder within the perforation to the crystalline density of the material. Theoretically, a packing fraction of 0.67 is possible for mono-sized spherical particles, but particle shape irregularities, interparticle and particle-sidewall friction, agglomeration, and internal powder porosity tend to reduce the packing fraction for powders [21]. The enrichment of  $^6\text{Li}$  and  $^{10}\text{B}$  in the conversion material was assumed to be 95%. For the  $^{10}\text{B}$ -backfilled DS-MSNDs unit cells with widths of 4, 6, 8, 10, and 12  $\mu\text{m}$  with feature depths of 20, 40, 60, and 80  $\mu\text{m}$  were considered. The feature depths represent 0.5, 1, 1.5, and 2 mean-free-path lengths for incident thermal neutrons given a macroscopic cross-section of 249  $\text{cm}^{-1}$  for  $^{10}\text{B}$  powder with an effective density of 1.075  $\text{g cm}^{-3}$ . The  $^6\text{LiF}$ -backfilled DS-MSNDs simulated herein had unit cell widths of 20, 40, 60, 80, and 100  $\mu\text{m}$  and perforation depths of 175, 350, 500, and 650  $\mu\text{m}$  representing 0.5, 1, 1.4, and 1.9 mean-free-path lengths for incident thermal neutrons given a macroscopic cross-section of 28.7  $\text{cm}^{-1}$  for 95%-enriched  $^6\text{LiF}$  powder with a density of 1.27  $\text{g cm}^{-3}$ .  $^6\text{LiF}$  powder has a substantially lower neutron absorption cross-section, requiring trench depths five to 10 times greater than  $^{10}\text{B}$ -filled counterparts to achieve similar detection efficiencies. However, the Q-value of the  $^6\text{Li}(n, t)^4\text{He}$  reaction is nearly double that of the  $^{10}\text{B}(n, \alpha)^7\text{Li}$  reaction resulting in combined reaction product ranges in the conversion material and Si approximately six times greater for  $^6\text{Li}$ -based devices. Longer reaction product ranges allow for larger features and less challenging device fabrication. Furthermore, the higher-energy reaction products are easier to distinguish from background noise and gamma-ray radiation events through pulse height discrimination alone. For all DS-MSND patterns, the ratio of the critical dimension of the microfeature, either trench width,  $T$ , or hole or pillar diameter,  $D$ , to the width of the unit cell,  $W_{\text{cell}}$ , was varied from 0.1 to 0.9. Table 1 outlines the parameters of the DS-MSND optimization study.

The intrinsic thermal-neutron detection efficiency was defined as the number of particle histories wherein more than 300 keV of energy is deposited into the Si substrate, divided by the total number of particle histories. A simulated parallel beam of 0.0253 eV neutrons was made to perpendicularly intersect the front face of the DS-MSND. The energy deposited in the semiconductor substrate, defined as natural Si, from the charged particle reaction products was tallied for each history. The Si substrate was populated with microstructures using macro-body definitions and repeating lattice structures, as demonstrated in Figs. 2, 10, 18, 26, and 28. Further details on construction of the structures can be found in their respective sections. MCNP6 has combined the abilities of MCNP5 and MCNPX to properly model the tracking of neutrons, their

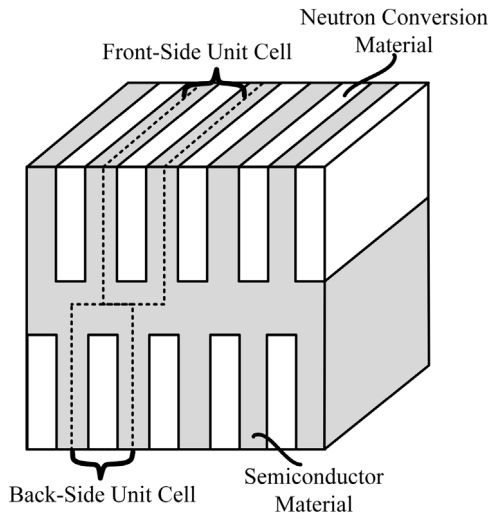


Fig. 2. The basic concept for a straight-trenched dual-sided microstructured semiconductor neutron detector (DS-MSND). Shown are two typical unit cells for the structure.

absorption within the conversion material, and the subsequent emission of the proper charged-particle reaction products and branching ratios. Reaction products were produced using the neutron capture ion algorithm (NCIA = 5), the reaction-product motion was tracked, and energy deposition was recorded within the proper tally volumes. An F8:T,A or F8:A,# tally was used to record and bin energy deposition from the reaction products in the active silicon thereby forming the pulse height spectrum. All events that deposited more 300 keV energy in the silicon features were summed to calculate the intrinsic thermal-neutron detection efficiency. It is assumed throughout this work that all energy deposited within the Si substrate is collected and measured by 'perfect' charge collection and detector electronics. Further details on the method by which the intrinsic thermal-neutron detection efficiency is defined within this work can also be found elsewhere [22]. Other than using NCIA for reaction production, default physics were used for neutron and heavy charged particle (triton, alpha,  $^7\text{Li}$ -ion) transport. Analog neutron capture was implemented with a CUT:N 2J 0 command, and the cutoff energy for the reaction products was set to 10 keV. All simulations were performed until a relative error less than or equal to 0.001 was achieved.

### 3. Offset-pattern perforation cases

The following section will consider devices wherein the front-side pattern is off-set by one-half of the unit-cell dimension and repeated on the back-side of the device. Three basic designs are investigated here: (1) a lateral matrix of straight, parallel trenches (the "trench design"), (2) a square matrix of cylindrical hole perforations (the "hole design"), and (3) a square matrix of cylindrical pillars that remain after etching bulk semiconductor material (the "pillar design").

#### 3.1. Straight trench-shaped perforations

Most DS-MSNDs presently fabricated utilize the straight-trench pattern, similar to those shown in Fig. 2. The pattern is simple to manufacture using common wet-etching techniques and allows for simple junction doping for good diode characteristics. The pattern also allows for simple formation of opaque DS-MSNDs as the pattern can be made to completely overlap itself on the opposing face. Reaction products generated within the trenches have a good probability of depositing energy into the substrate, provided that the width of the trenches does not exceed that of the summed ranges of the Li and  $\alpha$  ions, as

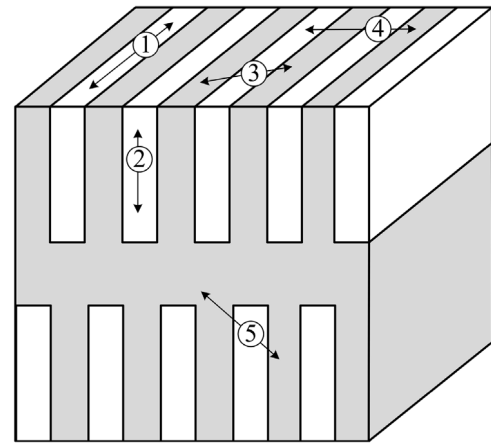


Fig. 3. Depicted are several of the trajectories for reaction products in a trench design DS-MSND. Here, (1) and (2) show complete misses where reaction products are not measured, (3) one or both reaction products are measured, (4) with small dimensions, one or both reaction products traverse another absorber, reduces energy deposited into the semiconductor. Also, (5) shows that reaction can occur in the backside trenches.

Table 1

Overview of parameters used in MCNP6 simulations.

Parameter	$^6\text{LiF}$	$^{10}\text{B}$
Wafer thickness	1500 $\mu\text{m}$	500 $\mu\text{m}$
Microfeature depth	175–650 $\mu\text{m}$	20–80 $\mu\text{m}$
Unit cell width	20–100 $\mu\text{m}$	4–12 $\mu\text{m}$
Microfeature-Width-to-Cell-Width Ratio	0.1–0.9	0.1–0.9
Backfill material	$^6\text{LiF}$	$^{10}\text{B}$
Backfill material enrichment	95%	95%
Packing fraction	50%	50%
Charge collection efficiency	100%	100%
Neutron energy	0.0253 eV	0.0253 eV

depicted in Fig. 3. Here, the reaction products from the  $^{10}\text{B}(n, \alpha)^7\text{Li}$  or  $^6\text{Li}(n, t)^4\text{He}$  reactions are emitted isotropically with the reaction products traveling in opposite directions. Fig. 3 shows the notable directions: (1) along the length of the trenches where no energy will be deposited into the semiconductor and fail to produce a count, (2) along the height of the trenches where no energy will be deposited into the semiconductor and fail to produce a count, (3) where one or both reaction products are fully stopped in the semiconductor medium, likely producing a count, (4) where one or both reaction products can traverse the semiconductor into another absorber, depositing little energy into the substrate, possibly producing a count, and (5) where similar reactions can occur in the back-side trenches. Cases (3), (4), and (5) are preferred.

#### 3.1.1. Efficiencies of $^{10}\text{B}$ -filled trenches

The calculated intrinsic thermal-neutron detection efficiencies of the  $^{10}\text{B}$ -filled straight-trenched DS-MSNDs for an LLD setting of 300 keV are given in Table 2. From Table 2, there is a general trend in the detection efficiency for a given trench depth and cell width. As the ratio of the trench width  $T$  to the cell width  $W_{\text{Cell}}$  increases, the neutron absorption efficiency of the device increases, leading to a general increase in detection efficiency. However, as the trench width is increased, the width of the silicon fin surrounding the trench is diminished and so too is the energy deposition from the reaction products into the silicon. After some optimal thickness of trenches is exceeded, the energy deposition into the silicon from the reaction products is reduced below the LLD threshold. It appears that the optimal detection efficiency occurs for a trench-to-cell-width ratio of 0.5 to 0.8 depending on trench depth for a 4- $\mu\text{m}$  wide unit cell, however, fabrication of such a device is problematic due to difficulty in etching and diffusing contacts into such

**Table 2**

Efficiencies for off-set straight trenches of width, T, and depth, H, filled with <sup>10</sup>B in a unit cell of width, W\_Cell. Neutrons are incident normally on the detector surface and the LLD cutoff energy is 300 keV.

Off-set dual-sided MSND, straight trench, 10-B					
T/W_Cell	Cell width W_Cell (μm)				
	4	6	8	10	12
Trench depth H = 20 μm					
0.10	7.4%	7.3%	7.2%	7.1%	7.1%
0.20	14.5%	14.1%	13.8%	13.4%	13.1%
0.30	21.2%	20.4%	19.6%	18.8%	18.2%
0.40	27.5%	26.2%	24.8%	23.4%	22.2%
0.50	33.5%	31.4%	29.3%	27.3%	25.4%
0.60	36.5%	33.6%	30.7%	27.9%	25.3%
0.70	39.4%	35.7%	32.1%	28.6%	25.2%
0.80	41.9%	37.7%	33.2%	28.9%	24.6%
0.90	27.3%	23.7%	23.0%	23.2%	23.8%
Trench depth H = 40 μm					
0.10	12.0%	11.9%	11.7%	11.6%	11.4%
0.20	23.5%	22.9%	22.3%	21.8%	21.2%
0.30	34.3%	33.1%	31.8%	30.4%	29.3%
0.40	44.6%	42.3%	40.0%	37.8%	35.6%
0.50	54.3%	50.7%	47.2%	43.8%	40.4%
0.60	56.3%	51.5%	46.8%	42.1%	37.5%
0.70	58.6%	52.7%	46.8%	41.1%	35.4%
0.80	60.6%	53.7%	46.8%	39.8%	33.0%
0.90	36.3%	30.6%	29.6%	29.9%	30.6%
Trench depth H = 60 μm					
0.10	14.9%	14.7%	14.5%	14.3%	14.1%
0.20	29.0%	28.3%	27.6%	26.9%	26.2%
0.30	42.4%	40.8%	39.2%	37.6%	36.1%
0.40	55.1%	52.3%	49.4%	46.6%	43.9%
0.50	67.1%	62.6%	58.2%	53.9%	49.6%
0.60	67.5%	61.6%	55.7%	49.8%	44.1%
0.70	68.5%	61.3%	54.2%	47.2%	40.2%
0.80	69.3%	61.1%	52.9%	44.6%	36.6%
0.90	39.8%	32.9%	31.8%	32.2%	33.0%
Trench depth H = 80 μm					
0.10	16.7%	16.5%	16.2%	16.0%	15.8%
0.20	32.4%	31.6%	30.9%	30.1%	29.3%
0.30	47.4%	45.6%	43.9%	42.0%	40.4%
0.40	61.6%	58.4%	55.2%	52.1%	49.0%
0.50	75.0%	70.0%	65.0%	60.2%	55.3%
0.60	74.1%	67.4%	60.9%	54.3%	47.9%
0.70	73.8%	66.0%	58.2%	50.4%	42.8%
0.80	73.6%	64.7%	55.8%	46.8%	38.2%
0.90	41.1%	33.7%	32.6%	33.0%	33.8%

**Table 3**

Efficiencies for off-set straight trenches of width, T, and depth, H, filled with <sup>6</sup>LiF in a unit cell of width, W\_Cell. Neutrons are incident normally on the detector surface and the LLD cutoff energy is 300 keV.

Off-set dual-sided MSND, straight trench, 6-LiF					
T/W_Cell	Cell width W_Cell (μm)				
	20	40	60	80	100
Trench depth H = 175 μm					
0.10	7.7%	7.5%	7.4%	7.3%	7.2%
0.20	15.0%	14.5%	14.0%	13.6%	13.1%
0.30	22.1%	21.0%	20.0%	19.0%	18.0%
0.40	29.0%	27.1%	25.3%	23.6%	22.0%
0.50	35.5%	32.6%	30.0%	27.5%	24.9%
0.60	39.1%	35.3%	31.7%	28.2%	24.8%
0.70	42.7%	37.8%	33.3%	28.9%	24.4%
0.80	46.0%	40.2%	34.6%	29.0%	24.1%
0.90	44.5%	35.2%	34.9%	28.8%	24.0%
Trench depth H = 350 μm					
0.10	12.4%	12.2%	12.0%	11.8%	11.6%
0.20	24.3%	23.6%	22.8%	22.0%	21.3%
0.30	35.8%	34.0%	32.4%	30.7%	29.1%
0.40	46.8%	43.8%	40.8%	38.0%	35.3%
0.50	57.4%	52.8%	48.3%	43.9%	39.7%
0.60	60.5%	54.3%	48.4%	42.6%	36.8%
0.70	63.7%	56.1%	48.8%	41.7%	34.5%
0.80	66.5%	57.6%	48.9%	40.3%	32.6%
0.90	62.4%	48.4%	47.9%	38.5%	31.2%
Trench depth H = 500 μm					
0.10	15.0%	14.8%	14.6%	14.3%	14.1%
0.20	29.4%	28.5%	27.5%	26.6%	25.8%
0.30	43.2%	41.1%	39.1%	37.1%	35.2%
0.40	56.5%	52.9%	49.3%	45.8%	42.5%
0.50	69.3%	63.7%	58.3%	52.9%	47.6%
0.60	71.2%	63.8%	56.6%	49.6%	42.6%
0.70	73.3%	64.4%	55.9%	47.4%	38.9%
0.80	75.1%	64.9%	54.8%	44.8%	35.8%
0.90	69.1%	53.2%	52.6%	42.0%	33.6%
Trench depth H = 650 μm					
0.10	16.8%	16.5%	16.3%	16.0%	15.7%
0.20	32.8%	31.8%	30.7%	29.7%	28.7%
0.30	48.1%	45.8%	43.6%	41.3%	39.1%
0.40	62.9%	58.9%	54.9%	51.0%	47.2%
0.50	77.1%	70.9%	64.8%	58.8%	52.9%
0.60	77.9%	69.7%	61.8%	54.0%	46.2%
0.70	79.0%	69.3%	60.0%	50.7%	41.4%
0.80	79.9%	68.8%	58.0%	47.2%	37.5%
0.90	72.4%	55.5%	54.9%	43.5%	34.7%

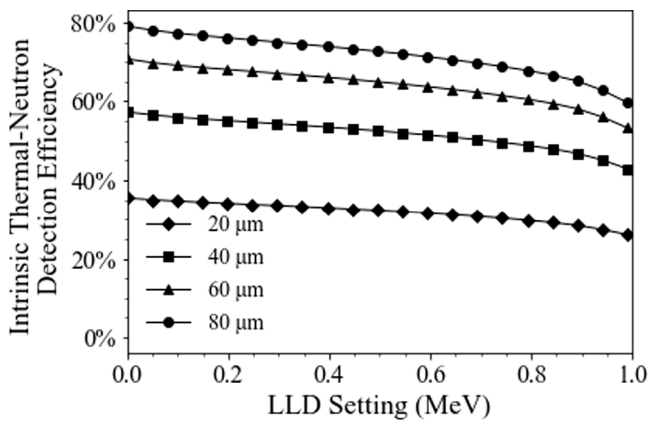


**Fig. 4.** Plotted are intrinsic thermal-neutron detection efficiencies for various perforation depths for the straight-trench design with 4-μm-wide unit cell and 2-μm-wide trenches backfilled with <sup>10</sup>B.

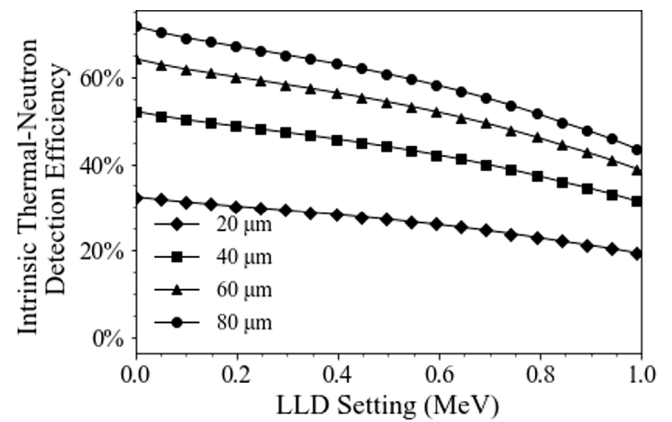


**Fig. 5.** Plotted are intrinsic thermal-neutron detection efficiencies for various perforation depths for the straight-trench design with 8-μm-wide unit cell and 4-μm-wide trenches backfilled with <sup>10</sup>B.

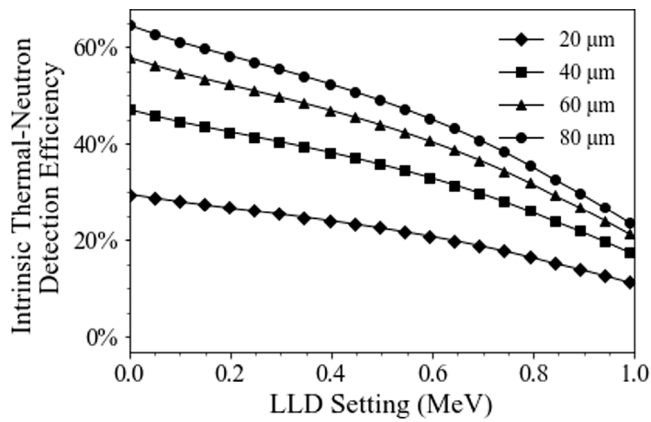


Fig. 6. Plotted are intrinsic thermal-neutron detection efficiencies for various perforation depths for the straight-trench design with 12- $\mu\text{m}$ -wide unit cell and 6- $\mu\text{m}$ -wide trenches backfilled with <sup>10</sup>B.

small features. The maximum detection efficiency occurs at the 0.5 trench-to-cell-width-ratio mark and is 75.0% for an 80- $\mu\text{m}$  deep trench.

Shown in Fig. 4 are the calculated intrinsic thermal-neutron detection efficiencies as a function of LLD setting where the unit cell is 4- $\mu\text{m}$  wide and the trenches are 2- $\mu\text{m}$  wide (i.e.  $T/W_{cell} = 0.5$ ). The zero LLD condition is the highest possible efficiency, ranging from 35.5% for 20- $\mu\text{m}$ -deep trenches to 79.0% for 80- $\mu\text{m}$ -deep trenches. Fig. 5 shows the calculated intrinsic thermal-neutron detection efficiencies as a function of LLD setting where the unit cell is 8- $\mu\text{m}$  wide and the trenches are 4- $\mu\text{m}$  wide (i.e.  $T/W_{cell} = 0.5$ ). With an LLD setting of 0 keV, the intrinsic detection efficiency is maximized at 32.4% for the 20- $\mu\text{m}$ -deep trenches and 71.6% intrinsic efficiency for the 80- $\mu\text{m}$ -deep trenches. Finally, Fig. 6 depicts the calculated intrinsic thermal-neutron detection efficiencies as a function of LLD setting where the unit cell is 12- $\mu\text{m}$  wide and the trenches are 6- $\mu\text{m}$  wide (i.e.  $T/W_{cell} = 0.5$ ). The intrinsic detection efficiency for these devices ranges from 29.6% to 64.5% for trenches etched depths of 20  $\mu\text{m}$  and 80  $\mu\text{m}$ , respectively.

### 3.1.2. Efficiencies of <sup>6</sup>LiF-filled trenches

The calculated intrinsic thermal-neutron detection efficiencies of the <sup>6</sup>LiF-filled straight-trenched DS-MSNDs for an LLD setting of 300 keV are given in Table 3. Similar to the results from the previous section, there is a trend of increasing intrinsic thermal-neutron detection efficiency with increasing  $T/W_{cell}$  ratio to 0.8 for small unit cell dimensions and approximately 0.5 for larger unit cell dimensions, and then the efficiency decreases beyond that point. A maximum theoretical detection efficiency of 79.9% is possible with a unit cell of 20  $\mu\text{m}$  and a trench-to-unit cell ratio of 0.8 for 650- $\mu\text{m}$  deep trenches. Unfortunately, the most optimum design requires the 650- $\mu\text{m}$  tall fins to be only 4- $\mu\text{m}$  wide, which poses significant fabrication challenges. However, deep-trench, high-aspect ratio DS-MSNDs with 30- $\mu\text{m}$  wide unit cells have been successfully fabricated [17,18,20].

Shown in Fig. 7 are the calculated intrinsic thermal-neutron detection efficiencies as a function of LLD setting where the unit cell is 20- $\mu\text{m}$  wide and the trenches are 14- $\mu\text{m}$  wide (i.e.  $T/W_{cell} = 0.7$ ). A maximum detection efficiency of 43.5% is calculated for trench depths of 175  $\mu\text{m}$  and zero LLD, while the maximum detection efficiency of the 650- $\mu\text{m}$  deep case is 80.1%. Fig. 8 shows the calculated intrinsic thermal-neutron detection efficiencies as a function of LLD setting where the unit cell is 60- $\mu\text{m}$  wide and the trenches are 30- $\mu\text{m}$  wide (i.e.  $T/W_{cell} = 0.5$ ). The detection efficiency ranges from 30.9% to 66.6% for the 175- $\mu\text{m}$  and the 650- $\mu\text{m}$  deep simulations, respectively. Finally, Fig. 9 depicts the calculated intrinsic thermal-neutron detection efficiencies as a function of LLD setting where the unit cell is 100- $\mu\text{m}$  wide and the trenches are 50- $\mu\text{m}$  wide (i.e.  $T/W_{cell} = 0.5$ ). The effect of energy loss in the conversion material is apparent as the zero LLD

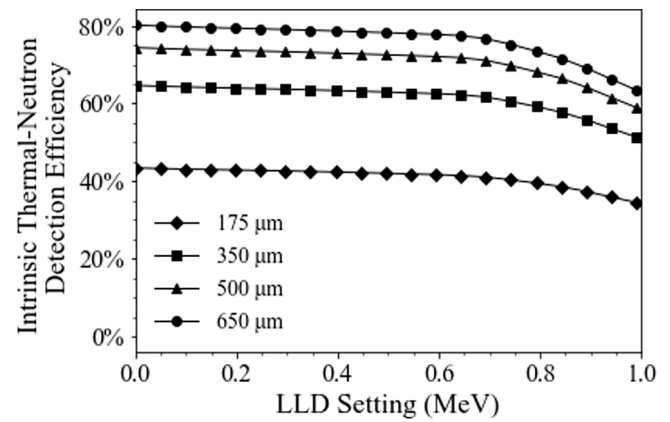


Fig. 7. Plotted are intrinsic thermal-neutron detection efficiencies for various perforation depths for the straight-trench design with 20- $\mu\text{m}$  wide unit cell and 14- $\mu\text{m}$  wide trenches backfilled with <sup>6</sup>LiF.

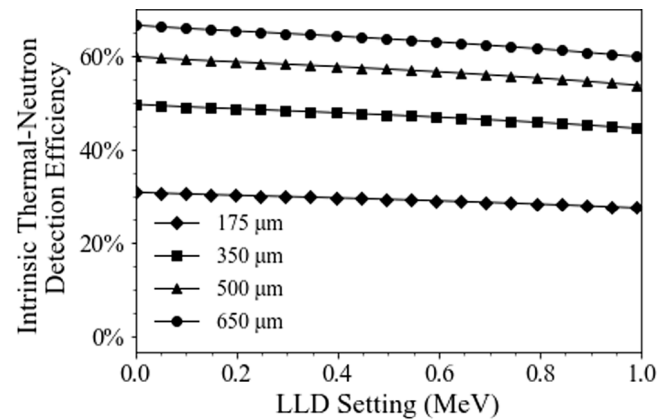


Fig. 8. Plotted are intrinsic thermal-neutron detection efficiencies for various perforation depths for the straight-trench design with 60- $\mu\text{m}$  unit cell and 30- $\mu\text{m}$  wide trenches backfilled with <sup>6</sup>LiF.

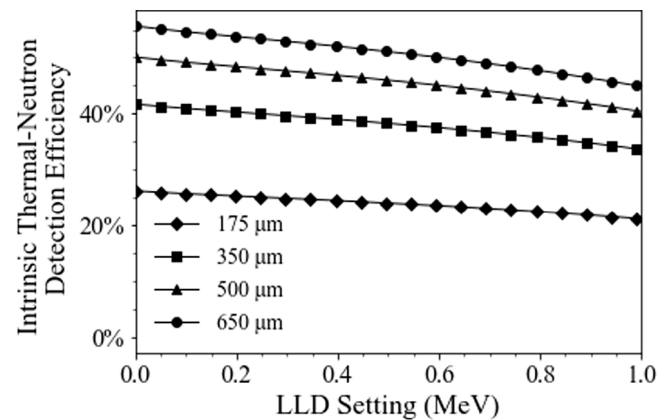


Fig. 9. Plotted are intrinsic thermal-neutron detection efficiencies for various perforation depths for the straight-trench design with 100- $\mu\text{m}$  unit cell and 50- $\mu\text{m}$  wide trenches backfilled with <sup>6</sup>LiF.

intrinsic detection efficiency is reduced to 26.2% and 55.6% for the 175- $\mu\text{m}$  and 650- $\mu\text{m}$  deep simulations, respectively.

### 3.2. Circular hole-shaped perforations

Circular-hole shaped perforations represented the earliest MSNDs produced replacing thin-film-coated neutron detectors (Fig. 10) [9] and

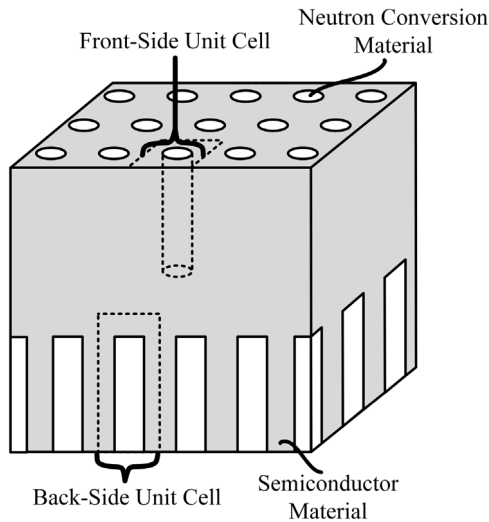


Fig. 10. The basic concept for a circular-hole dual-sided microstructured semiconductor neutron detector (DS-MSND). Shown are two typical unit cells for the structure.

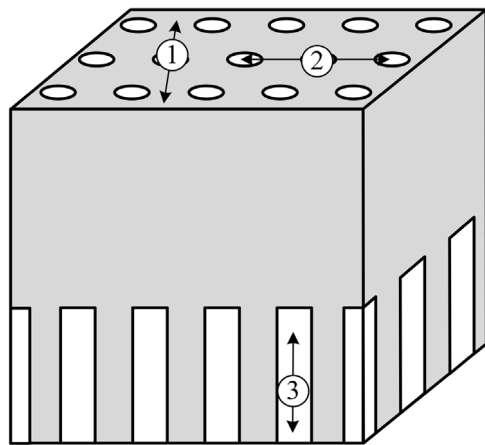


Fig. 11. Depicted are several of the trajectories for reaction products in a hole design DS-MSND. Here, (1) shows complete absorptions where reaction products are fully measured, (2) one or both reaction products are absorbed in an adjacent hole structure, failing to fully energize the substrate, and (3) with large dimensions, one or both reaction products fail to exit the hole, failing to be counted.

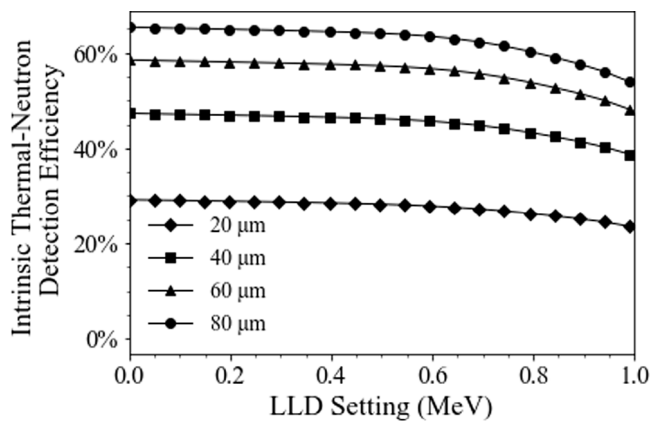


Fig. 12. Plotted are intrinsic thermal-neutron detection efficiencies for various perforation depths for the circular-hole design with 4-μm unit cell and 2.8-μm diameter holes backfilled with <sup>10</sup>B.

have been investigated further by other groups [23,24]. Devices using these perforations are simple to fabricate using standard ICP-RIE etching techniques and do not require alignment to specific crystal planes for etching. Conformal diffusion and contact formation on these devices are also simple and the electric field established with the device often assures good charge-collection efficiency. However, offset style, circular hole-geometry DS-MSNDs can only be fully opaque to normally incident neutrons if the hole diameter is equal to the unit cell width. If the hole diameter is less than the unit cell width streaming paths through the bulk silicon exist where normally incident neutrons can pass through the detector without intersecting any neutron conversional material on either side of the device. Furthermore, the total interaction probability of a normally incident thermal neutron (0.0253) in silicon is less than 1% for 500-μm thick detectors and less than 2% for 1500-μm thick detectors. The hole pattern benefits from excellent reaction-product detection efficiency for holes with a diameter less than the combined ranges of the reaction products, leading to devices that can have high LLD-settings without great detriment to the detection efficiency. Fig. 11 shows the various paths that the charged reaction products can follow from a neutron-capture reaction. Case (1) shows the likely scenarios where complete absorptions of both reaction products occurs. Case (2) depicts one or both reaction products traversing the substrate into an adjacent hole, failing to fully deposit their energies into the substrate, reducing the pulse height. Case (3) is the least likely case to occur, showing one or both reaction products being emitted along the length of the hole, being reabsorbed in the conversion material. The probability of Case 3 scenarios can be reduced with smaller hole features.

### 3.2.1. Efficiencies of <sup>10</sup>B-filled holes

The calculated intrinsic thermal-neutron detection efficiencies of the <sup>10</sup>B-filled circular-holes etched into the DS-MSNDs for an LLD setting of 300 keV are given in Table 4. From Table 4, there is a general trend of increasing detection efficiency for an increasing  $D/W_{Cell}$  ratio. As the ratio of the hole diameter,  $D$ , to the cell width,  $W_{Cell}$ , increases, the neutron absorption efficiency of the device increases, leading to a general increase in detection efficiency. Similar to the trenched devices, the thickness of the silicon surrounding the hole is diminished and so too is the energy deposition from the reaction products into the silicon. After some optimal hole diameter is exceeded, the energy deposition into the silicon from the reaction products is reduced below the LLD threshold. It appears that the optimal detection efficiency occurs for a hole-to-cell-width near 0.9 for a 4-μm wide unit cell, however, fabrication of such a device is problematic due to difficulty in etching and diffusing contacts into such small and high aspect ratio features. Unlike the trenched devices, the hole-shaped perforations do not suffer greatly from self-absorption of neutrons in the front-side to back-side feature from perforation overlap.

Shown in Fig. 12 are the calculated intrinsic thermal-neutron detection efficiencies as a function of LLD setting where the unit cell is 4-μm wide and the holes have a diameter of 2.8 μm (i.e.  $D/W_{cell} = 0.7$ ). The zero LLD condition is the highest possible efficiency, ranging from 29.2% for 20-μm deep trenches to 65.4% for 80-μm deep holes. Fig. 13 shows the calculated intrinsic thermal-neutron detection efficiencies as a function of LLD setting where the unit cell is 8-μm wide and the holes are 5.6-μm wide (i.e.  $D/W_{cell} = 0.7$ ). With an LLD setting of 0 keV, the intrinsic detection efficiency is maximized at 28.4% for the 20-μm deep holes and 63.8% intrinsic efficiency for the 80-μm deep holes. Finally, Fig. 14 depicts the calculated intrinsic thermal-neutron detection efficiencies as a function of LLD setting where the unit cell is 12-μm wide and the holes are 8.4-μm in diameter (i.e.  $D/W_{cell} = 0.7$ ). The intrinsic detection efficiency for these devices ranges from 27.2% for holes etched to 20 μm and 61.1% for holes etched to 80 μm. The decrease in detection efficiency versus LLD setting is much more rapid for these devices, indicative of the poor energy deposition in the silicon due to losses in the thicker conversion material layers.

**Table 4**

Efficiencies for off-set circular holes of diameter D and depth H filled with <sup>10</sup>B in a unit cell of width W<sub>cell</sub>. Neutrons are incident normally on the detector surface and the LLD cutoff energy is 300 keV.

Off-set dual-sided MSND, circular hole, 10-B					
D/W_Cell	Cell width W_Cell (μm)				
	4	6	8	10	12
Trench depth H = 20 μm					
0.10	0.6%	0.6%	0.6%	0.6%	0.6%
0.20	2.4%	2.4%	2.4%	2.4%	2.4%
0.30	5.4%	5.4%	5.3%	5.3%	5.2%
0.40	9.5%	9.5%	9.4%	9.2%	9.1%
0.50	14.8%	14.7%	14.4%	14.1%	13.8%
0.60	21.2%	20.9%	20.4%	19.9%	19.2%
0.70	28.7%	28.1%	27.3%	26.3%	25.0%
0.80	35.9%	34.9%	33.5%	31.9%	29.1%
0.90	41.1%	38.1%	36.0%	35.0%	31.4%
Trench depth H = 40 μm					
0.10	1.0%	1.0%	1.0%	1.0%	1.0%
0.20	3.9%	3.9%	3.9%	3.9%	3.9%
0.30	8.7%	8.7%	8.6%	8.6%	8.5%
0.40	15.5%	15.4%	15.2%	15.0%	14.9%
0.50	24.1%	23.8%	23.5%	23.0%	22.5%
0.60	34.5%	34.0%	33.3%	32.4%	31.3%
0.70	46.7%	45.7%	44.4%	42.8%	40.6%
0.80	57.1%	55.5%	53.3%	50.5%	45.7%
0.90	62.9%	57.9%	54.5%	52.6%	46.6%
Trench depth H = 60 μm					
0.10	1.2%	1.2%	1.2%	1.2%	1.2%
0.20	4.8%	4.8%	4.8%	4.8%	4.8%
0.30	10.8%	10.8%	10.7%	10.7%	10.6%
0.40	19.2%	19.1%	18.9%	18.6%	18.4%
0.50	29.8%	29.5%	29.1%	28.6%	28.0%
0.60	42.7%	42.1%	41.2%	40.1%	38.7%
0.70	57.8%	56.6%	55.1%	53.0%	50.2%
0.80	69.6%	67.7%	65.1%	61.4%	55.3%
0.90	74.7%	68.5%	64.4%	62.0%	54.6%
Trench depth H = 80 μm					
0.10	1.4%	1.4%	1.4%	1.4%	1.4%
0.20	5.4%	5.4%	5.4%	5.4%	5.4%
0.30	12.1%	12.1%	12.0%	11.9%	11.9%
0.40	21.4%	21.3%	21.1%	20.9%	20.6%
0.50	33.3%	33.0%	32.6%	32.0%	31.3%
0.60	47.8%	47.1%	46.2%	44.9%	43.4%
0.70	64.7%	63.4%	61.6%	59.3%	56.1%
0.80	77.1%	75.1%	72.1%	68.0%	61.2%
0.90	81.4%	74.5%	69.9%	67.2%	59.0%

**Table 5**

Efficiencies for off-set circular holes of diameter D and depth H filled with <sup>6</sup>LiF in a unit cell of width W<sub>cell</sub>. Neutrons are incident normally on the detector surface and the LLD cutoff energy is 300 keV.

Off-set dual-sided MSND, circular hole, 6-LiF					
D/W_Cell	Cell width W_Cell (μm)				
	20	40	60	80	100
Trench depth H = 175 μm					
0.10	0.6%	0.6%	0.6%	0.6%	0.6%
0.20	2.4%	2.4%	2.4%	2.4%	2.4%
0.30	5.5%	5.4%	5.4%	5.3%	5.3%
0.40	9.7%	9.6%	9.5%	9.3%	9.2%
0.50	15.1%	14.8%	14.6%	14.3%	13.9%
0.60	21.7%	21.2%	20.7%	20.1%	19.1%
0.70	29.3%	28.6%	27.7%	26.5%	24.6%
0.80	36.7%	35.6%	34.2%	32.0%	28.3%
0.90	43.5%	41.1%	39.9%	36.2%	31.0%
Trench depth H = 350 μm					
0.10	1.0%	1.0%	1.0%	1.0%	1.0%
0.20	4.0%	4.0%	4.0%	3.9%	3.9%
0.30	8.9%	8.9%	8.8%	8.7%	8.6%
0.40	15.8%	15.6%	15.4%	15.2%	15.0%
0.50	24.6%	24.2%	23.8%	23.3%	22.6%
0.60	35.1%	34.5%	33.7%	32.7%	31.1%
0.70	47.5%	46.5%	45.0%	43.1%	39.7%
0.80	58.2%	56.7%	54.2%	50.6%	44.1%
0.90	66.4%	62.7%	60.7%	54.5%	46.0%
Trench depth H = 500 μm					
0.10	1.2%	1.2%	1.2%	1.2%	1.2%
0.20	4.8%	4.8%	4.8%	4.8%	4.8%
0.30	10.8%	10.8%	10.7%	10.6%	10.5%
0.40	19.1%	18.9%	18.7%	18.5%	18.1%
0.50	29.7%	29.3%	28.8%	28.2%	27.4%
0.60	42.5%	41.7%	40.8%	39.5%	37.6%
0.70	57.4%	56.2%	54.5%	52.1%	48.0%
0.80	69.4%	67.6%	64.6%	60.2%	52.3%
0.90	77.4%	73.1%	70.7%	63.3%	53.1%
Trench depth H = 650 μm					
0.10	1.4%	1.4%	1.4%	1.4%	1.3%
0.20	5.4%	5.4%	5.4%	5.3%	5.3%
0.30	12.1%	12.0%	11.9%	11.8%	11.7%
0.40	21.3%	21.1%	20.9%	20.6%	20.3%
0.50	33.1%	32.6%	32.1%	31.5%	30.5%
0.60	47.3%	46.5%	45.5%	44.1%	41.9%
0.70	63.9%	62.7%	60.7%	58.0%	53.4%
0.80	76.6%	74.6%	71.4%	66.4%	57.6%
0.90	84.2%	79.4%	76.8%	68.6%	57.3%

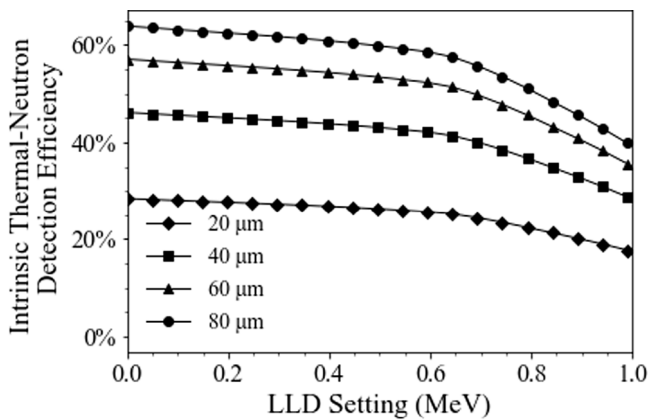


**Fig. 13.** Plotted are intrinsic thermal-neutron detection efficiencies for various perforation depths for the circular-hole design with 8-μm unit cell and 5.6-μm diameter holes backfilled with <sup>10</sup>B.

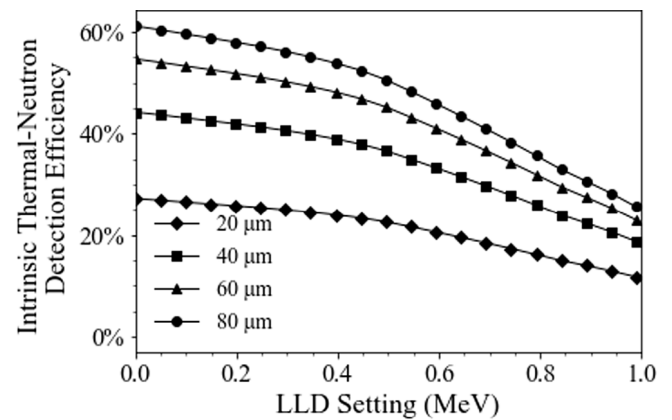


**Fig. 14.** Plotted are intrinsic thermal-neutron detection efficiencies for various perforation depths for the circular-hole design with 12-μm unit cell and 8.4-μm diameter holes backfilled with <sup>10</sup>B.

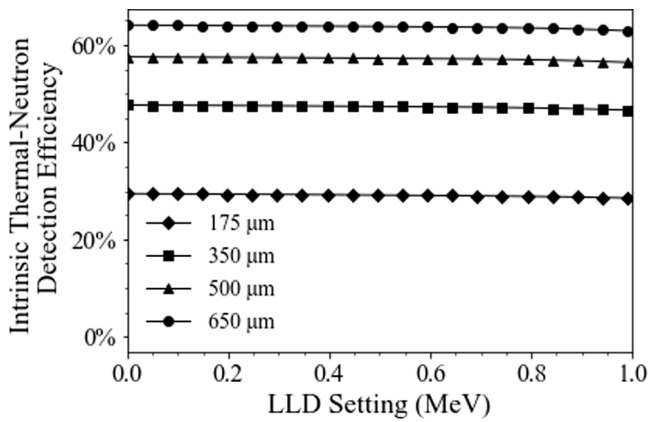


Fig. 15. Plotted are intrinsic thermal-neutron detection efficiencies for various perforation depths for the circular-hole design with 20- $\mu\text{m}$  unit cell and 14- $\mu\text{m}$  diameter holes backfilled with  $^6\text{LiF}$ .

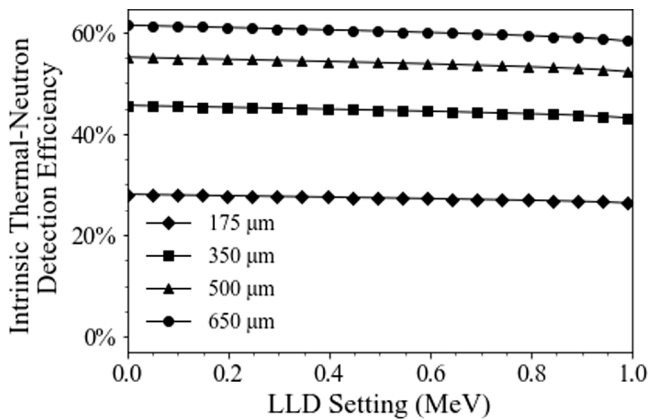


Fig. 16. Plotted are intrinsic thermal-neutron detection efficiencies for various perforation depths for the circular-hole design with 60- $\mu\text{m}$  unit cell and 42- $\mu\text{m}$  diameter holes backfilled with  $^6\text{LiF}$ .

### 3.2.2. Efficiencies of $^6\text{LiF}$ -filled holes

The calculated intrinsic thermal-neutron detection efficiencies of the  $^6\text{LiF}$ -filled circular-holes etched into the DS-MSNDs for an LLD setting of 300 keV are given in Table 5. From Table 5, there is a general trend of increasing detection efficiency for an increasing  $D/W_{\text{cell}}$  ratio. As the ratio of the hole diameter to the cell width increases, the neutron absorption efficiency of the device increases leading to a general increase in detection efficiency. Similar to the trenched devices, the thickness of the silicon surrounding the hole is diminished and so too is the energy deposition from the reaction products into the silicon, however, with the more energetic  $^6\text{Li}$  reaction products, the effect is not as prevalent as with the  $^{10}\text{B}$ -filled holes. The theoretical optimal detection efficiency occurs for a hole-to-cell-width ratio of 0.9 for a 20- $\mu\text{m}$  wide unit cell, however, fabrication of 2- $\mu\text{m}$  wide features is problematic due to difficulty in etching and diffusing contacts into small silicon features. The efficiency of these devices is less than their straight-trenched counterparts for reasonably fabricated feature sizes ( $D/W_{\text{cell}} \leq 0.7$ ) primarily due to the reduced presence of neutron conversion material resulting in neutron free streaming paths.

Shown in Fig. 15 are the calculated intrinsic thermal-neutron detection efficiencies as a function of LLD setting where the unit cell is 20- $\mu\text{m}$  wide and the holes have a diameter of 14  $\mu\text{m}$  (i.e.  $D/W_{\text{cell}} = 0.7$ ). The zero LLD condition is the highest possible efficiency, ranging from 29.5% for 175- $\mu\text{m}$ -deep holes to 64.1% for 650- $\mu\text{m}$ -deep holes. Fig. 16 shows the calculated intrinsic thermal-neutron detection efficiencies as a function of LLD setting where the unit cell is 60- $\mu\text{m}$  wide and the

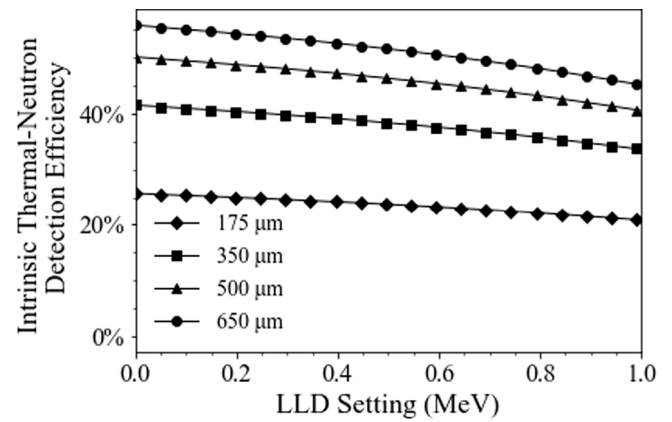


Fig. 17. Plotted are intrinsic efficiencies for various perforation depths for the circular-hole design with 100- $\mu\text{m}$  unit cell and 70- $\mu\text{m}$  diameter holes backfilled with  $^6\text{LiF}$ .

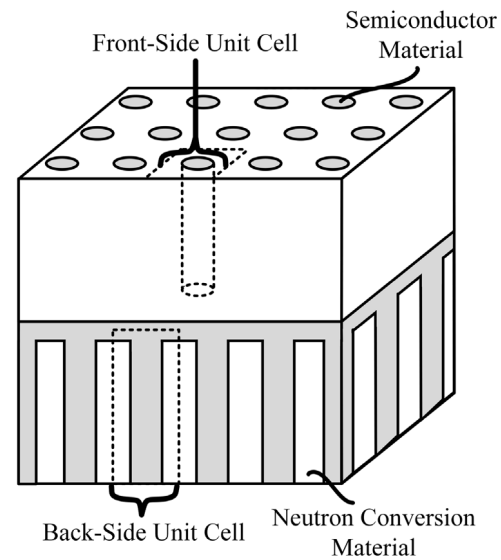


Fig. 18. The basic concept for a circular-pillar dual-sided microstructured semiconductor neutron detector (DS-MSND). Shown are two typical unit cells for the structure.

holes are 42- $\mu\text{m}$  wide (i.e.  $D/W_{\text{cell}} = 0.7$ ). With an LLD setting of 0 keV, the intrinsic detection efficiency is maximized at 28.1% for the 175- $\mu\text{m}$ -deep holes and 61.4% intrinsic efficiency for the 650- $\mu\text{m}$ -deep holes. Finally, Fig. 17 depicts the calculated intrinsic thermal-neutron detection efficiencies as a function of LLD setting where the unit cell is 100- $\mu\text{m}$  wide and the holes are 70  $\mu\text{m}$  in diameter (i.e.  $D/W_{\text{cell}} = 0.7$ ). The intrinsic detection efficiency for these devices ranges from 25.7% for holes etched to 175  $\mu\text{m}$  and 55.8% for holes etched to 500  $\mu\text{m}$ .

### 3.3. Circular pillar-shaped structures

Circular-pillar shaped perforations are a variation of the circular-type structures that has been previously investigated by other groups [25,26]. Devices using these perforations can be difficult to fabricate using standard ICP-RIE etching techniques due to the probability of etching away structures and the large amount of bulk material that must be removed (Fig. 18). Diffusion and blocking-contact formation on these devices can be challenging as a large amount of the bulk material is consumed by the dopant material and made blind to incident reaction products. Finally, forming electrical contact with all of the pillars simultaneously is difficult, thereby, leading to issues of utilizing

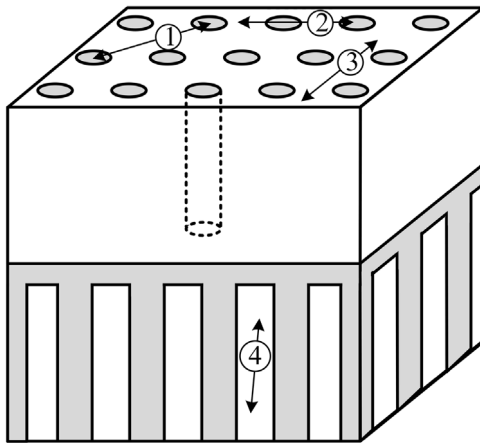


Fig. 19. Depicted are several of the trajectories for reaction products in a pillar design DS-MSND. (1) shows where both reaction products are measured, (2) one or both reaction products are absorbed in converter, (3) no energy is deposited into the silicon, and (4) interaction in back-side converter.

the entire diode. However, the large amount of neutron conversion material present can produce devices with high detection efficiencies and with low LLD settings.

Unlike with the circular-hole shaped pattern, pillar-type DS-MSNDs typically do not have neutron streaming paths present due to the large amount of neutron conversion material present. However, the pattern can suffer from poor reaction product detection efficiency from the small solid angle of the pillar structures as seen by the conversion material. Fig. 19 shows the various paths that the charged reaction products can follow from a neutron capture reaction. Case (1) shows the unlikely scenario where both reaction products are measured to some extent. Case (2) depicts one or both reaction products traversing the substrate and being absorbed in the conversion material, failing to fully deposit their energies into the substrate, reducing the pulse height. Case (3) shows one or both reaction products being emitted away from the pillar structures, being reabsorbed in the conversion material, failing to count that reaction product.

### 3.3.1. Efficiencies of <sup>10</sup>B-surrounded circular structures

The calculated intrinsic thermal-neutron detection efficiencies of the <sup>10</sup>B-surrounded circular pillars etched into the DS-MSNDs for an LLD setting of 300 keV are given in Table 6. From Table 6, the familiar trend of increasing detection efficiency for an increasing  $D/W_{Cell}$  ratio emerges. As the ratio of the pillar diameter to the cell width increases, the neutron absorption efficiency of the device decreases but is offset by the increasing density of the pillar structures improving the reaction product detection efficiency and ultimately leading to a general increase in detection efficiency. It appears that the optimal detection efficiency occurs for a hole-to-cell-width ratio of 0.7 for a 4- $\mu$ m wide unit cell, however, fabrication of such a device is problematic due to difficulty in etching and diffusing contacts into such small features. Furthermore, forming a continuous contact over the front- and back-side pillars but often comes at a cost of neutron absorption within the contact.

Shown in Fig. 20 are the calculated intrinsic thermal-neutron detection efficiencies as a function of LLD setting where the unit cell is 4  $\mu$ m wide and the pillars have a diameter of 2.8  $\mu$ m (i.e.  $D/W_{Cell} = 0.7$ ). The zero LLD condition is the highest possible efficiency, ranging from 43.6% for 20- $\mu$ m-deep etch to 82.1% for 80- $\mu$ m-tall pillars. A rapid decrease is observed in intrinsic detection efficiency with increased LLD setting. Fig. 21 shows the calculated intrinsic thermal neutron detection efficiencies as a function of LLD setting where the unit cell is 8- $\mu$ m wide and the pillars are 5.6- $\mu$ m wide (i.e.  $D/W_{Cell} = 0.7$ ). With a

Table 6

Efficiencies for off-set circular pillars of diameter  $D$  and depth  $H$  surrounded with <sup>10</sup>B in a unit cell of width  $W_{cell}$ . Neutrons are incident normally on the detector surface and the LLD cutoff energy is 300 keV.

Off-set dual-sided MSND, circular pillar, 10-B					
D/ $W_{Cell}$	Cell width $W_{Cell}$ ( $\mu$ m)				
	4	6	8	10	12
Trench depth $H = 20 \mu$ m					
0.10	5.9%	5.9%	6.3%	6.6%	7.1%
0.20	9.2%	9.2%	12.1%	11.4%	10.6%
0.30	19.2%	19.2%	16.8%	15.0%	13.5%
0.40	29.3%	29.3%	21.0%	18.4%	16.3%
0.50	35.5%	35.5%	24.8%	21.5%	19.1%
0.60	38.9%	38.9%	28.0%	24.3%	21.6%
0.70	39.7%	39.7%	30.7%	27.2%	24.2%
0.80	36.2%	36.2%	30.4%	27.9%	25.3%
0.90	28.8%	28.8%	26.1%	24.8%	23.2%
Trench depth $H = 40 \mu$ m					
0.10	3.5%	3.8%	4.2%	4.6%	5.3%
0.20	8.4%	11.7%	12.5%	11.4%	10.4%
0.30	23.0%	22.8%	19.5%	16.8%	14.6%
0.40	38.0%	31.1%	26.0%	22.1%	19.0%
0.50	48.3%	38.4%	32.4%	27.3%	23.7%
0.60	55.3%	44.9%	38.6%	32.7%	28.5%
0.70	59.1%	50.5%	44.9%	39.3%	34.3%
0.80	55.7%	50.5%	46.6%	42.5%	38.1%
0.90	45.1%	42.8%	40.8%	38.7%	36.1%
Trench depth $H = 60 \mu$ m					
0.10	2.1%	2.4%	2.9%	3.4%	4.1%
0.20	7.6%	11.3%	12.2%	10.9%	9.8%
0.30	24.0%	23.8%	20.1%	17.0%	14.5%
0.40	41.1%	33.4%	27.6%	23.1%	19.6%
0.50	53.6%	42.2%	35.4%	29.4%	25.1%
0.60	62.8%	50.7%	43.4%	36.3%	31.3%
0.70	69.2%	58.9%	52.3%	45.5%	39.4%
0.80	66.4%	60.1%	55.4%	50.5%	45.1%
0.90	54.3%	51.6%	49.1%	46.5%	43.4%
Trench depth $H = 80 \mu$ m					
0.10	1.3%	1.7%	2.2%	2.7%	3.4%
0.20	7.0%	10.9%	11.8%	10.5%	9.3%
0.30	24.1%	23.9%	20.1%	16.8%	14.2%
0.40	42.3%	34.2%	28.1%	23.3%	19.6%
0.50	55.9%	43.8%	36.6%	30.2%	25.6%
0.60	66.6%	53.5%	45.7%	38.0%	32.5%
0.70	74.7%	63.4%	56.3%	48.8%	42.1%
0.80	72.5%	65.5%	60.5%	55.0%	49.0%
0.90	59.6%	56.6%	53.9%	51.0%	47.5%

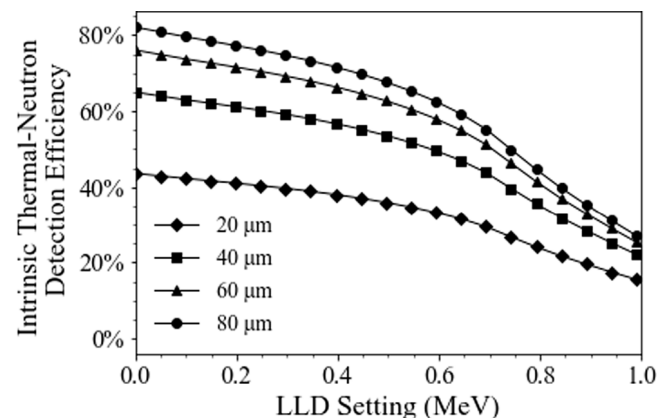


Fig. 20. Plotted are intrinsic thermal-neutron detection efficiencies for various perforation depths for the circular-pillar design with 4- $\mu$ m unit cell and 2.8- $\mu$ m diameter pillars surrounded with <sup>10</sup>B.

LLD setting of 0 keV, the intrinsic thermal-neutron detection efficiency is maximized at 36.5% for the 20- $\mu$ m-deep perforations and 67.1%

**Table 7**

Efficiencies for off-set circular pillars of diameter  $D$  and depth  $H$  surrounded with  ${}^6\text{LiF}$  in a unit cell of width  $W_{\text{cell}}$ . Neutrons are incident normally on the detector surface and the LLD cutoff energy is 300 keV.

Off-set dual-sided MSND, circular pillar, ${}^6\text{LiF}$					
D/ $W_{\text{Cell}}$	Cell width $W_{\text{Cell}}$ ( $\mu\text{m}$ )				
	20	40	60	80	100
Trench depth $H = 175 \mu\text{m}$					
0.10	8.0%	8.3%	8.9%	8.8%	8.3%
0.20	16.5%	17.3%	14.5%	12.6%	11.3%
0.30	30.7%	23.9%	19.1%	16.2%	14.1%
0.40	39.8%	29.0%	23.3%	19.5%	16.9%
0.50	42.7%	32.9%	26.7%	22.6%	19.6%
0.60	42.4%	35.3%	29.3%	25.2%	21.9%
0.70	40.3%	35.7%	30.7%	27.2%	24.0%
0.80	35.1%	32.5%	29.4%	27.1%	24.5%
0.90	27.1%	26.0%	24.5%	23.3%	21.9%
Trench depth $H = 350 \mu\text{m}$					
0.10	6.8%	7.3%	8.3%	8.1%	7.4%
0.20	19.8%	20.8%	16.7%	13.9%	11.8%
0.30	41.3%	30.8%	23.8%	19.5%	16.2%
0.40	55.6%	39.2%	30.6%	24.9%	20.8%
0.50	61.3%	46.2%	36.7%	30.3%	25.6%
0.60	62.8%	51.5%	42.0%	35.6%	30.3%
0.70	62.0%	54.7%	46.5%	40.9%	35.4%
0.80	55.5%	51.4%	46.4%	42.4%	38.1%
0.90	43.5%	41.8%	39.5%	37.4%	35.1%
Trench depth $H = 500 \mu\text{m}$					
0.10	6.0%	6.6%	7.7%	7.4%	6.6%
0.20	20.6%	21.7%	17.0%	13.9%	11.6%
0.30	45.0%	33.1%	25.2%	20.3%	16.6%
0.40	61.7%	43.0%	33.1%	26.8%	22.0%
0.50	69.0%	51.5%	40.6%	33.4%	27.8%
0.60	72.0%	58.7%	47.5%	40.1%	33.9%
0.70	72.7%	64.0%	54.3%	47.6%	41.0%
0.80	66.2%	61.3%	55.2%	50.5%	45.1%
0.90	52.4%	50.3%	47.5%	45.0%	42.2%
Trench depth $H = 650 \mu\text{m}$					
0.10	5.4%	6.1%	7.2%	6.8%	6.0%
0.20	20.8%	21.9%	17.0%	13.7%	11.3%
0.30	46.6%	34.0%	25.7%	20.5%	16.6%
0.40	64.7%	44.8%	34.3%	27.5%	22.5%
0.50	73.3%	54.3%	42.6%	34.9%	28.8%
0.60	77.4%	62.9%	50.7%	42.7%	35.9%
0.70	79.4%	69.8%	59.0%	51.7%	44.4%
0.80	73.1%	67.7%	60.9%	55.7%	49.7%
0.90	58.2%	55.9%	52.8%	50.0%	46.8%

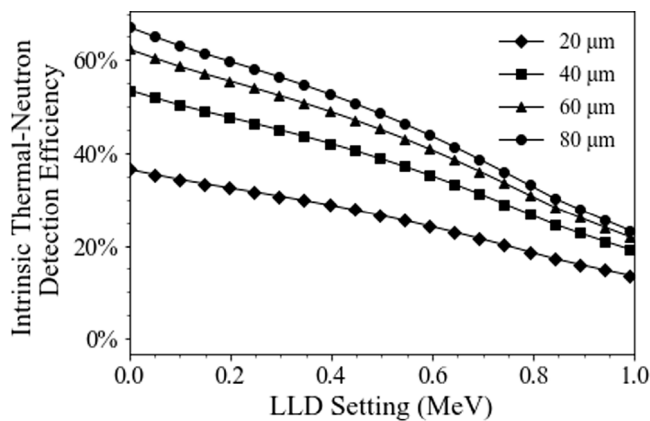


**Fig. 21.** Plotted are intrinsic thermal-neutron detection efficiencies for various perforation depths for the circular-pillar design with 8- $\mu\text{m}$  unit cell and 5.6- $\mu\text{m}$  diameter pillars surrounded with  ${}^{10}\text{B}$ .

intrinsic efficiency for the 60- $\mu\text{m}$ -tall pillars. The detection efficiency

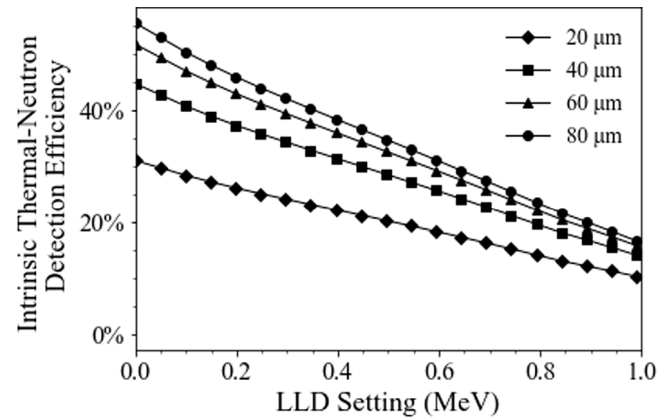


**Fig. 22.** Plotted are intrinsic thermal-neutron detection efficiencies for various perforation depths for the circular-pillar design with 12- $\mu\text{m}$  unit cell and 8.4- $\mu\text{m}$  diameter pillars surrounded with  ${}^{10}\text{B}$ .

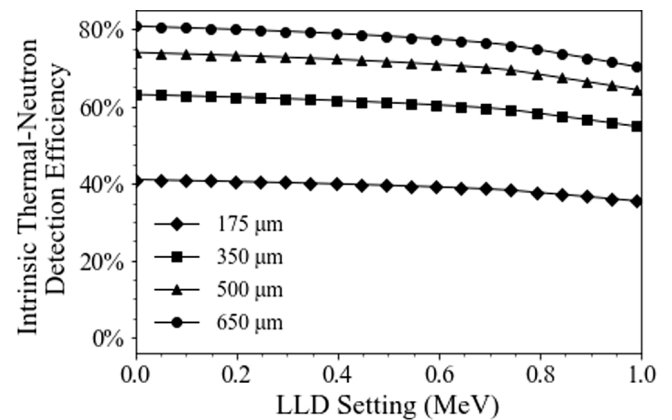


**Fig. 23.** Plotted are intrinsic thermal-neutron detection efficiencies for various perforation depths for the circular-pillar design with 20- $\mu\text{m}$  unit cell and 14- $\mu\text{m}$  diameter pillars surrounded with  ${}^6\text{LiF}$ .

is less dependent on the LLD than with the previous unit cell consideration. Finally, Fig. 22 depicts the calculated intrinsic thermal-neutron detection efficiencies as a function of LLD setting where the unit cell is 12- $\mu\text{m}$  wide and the pillars are 8.4- $\mu\text{m}$  in diameter (i.e.  $D/W_{\text{cell}} = 0.7$ ). The intrinsic detection efficiency for these devices ranges from 31.1% for perforations etched to 20  $\mu\text{m}$  and 55.6% for pillars 80- $\mu\text{m}$  tall. The reduced density of the pillar structures significantly reduces the overall detection efficiency even at the zero LLD setting.

### 3.3.2. Efficiencies of ${}^6\text{LiF}$ -surrounded circular structures

The calculated intrinsic thermal-neutron detection efficiencies of the  ${}^6\text{LiF}$ -surrounded circular pillars etched into the DS-MSNDs for an LLD setting of 300 keV are given in Table 7. From Table 7, increasing detection efficiency for an increasing  $D/W_{\text{Cell}}$  ratio is again seen up to a ratio of about 0.7. As the ratio of the pillar diameter to the cell width increases, the neutron absorption efficiency of the device decreases but is countered by the increasing density of the pillar structures that increase reaction product detection probability, leading to a general increase in detection efficiency. The reported results are a best-case scenario where in reality forming a continuous contact over the front- and back-side pillars will produce a region insensitive to charge-particles around the edge of all the pillars reducing the charge-particle detection efficiency and lowering the final pulse height.

Shown in Fig. 23 are the calculated intrinsic thermal-neutron detection efficiencies as a function of LLD setting where the unit cell is 20  $\mu\text{m}$  wide and the pillars have a diameter of 14  $\mu\text{m}$  (i.e.  $D/W_{\text{cell}} = 0.7$ ).

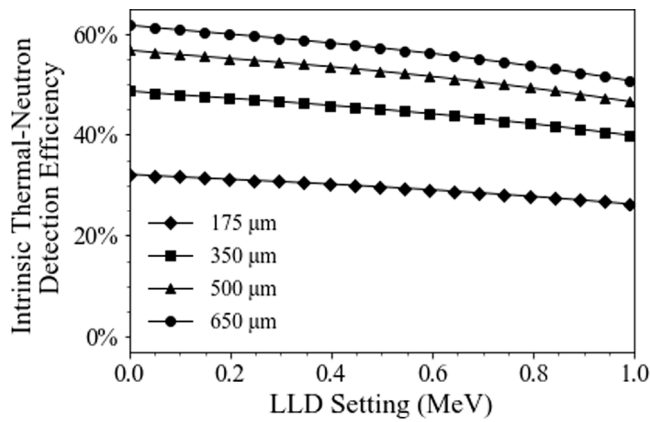


Fig. 24. Plotted are intrinsic thermal-neutron detection efficiencies for various perforation depths for the circular-pillar design with 60- $\mu\text{m}$  unit cell and 42- $\mu\text{m}$  diameter pillars surrounded with  ${}^6\text{LiF}$ .

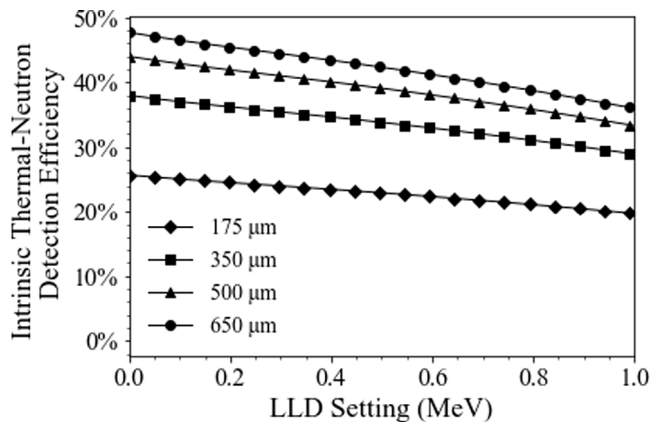


Fig. 25. Plotted are intrinsic thermal-neutron detection efficiencies for various perforation depths for the circular-pillar design with 100- $\mu\text{m}$  unit cell and 70- $\mu\text{m}$  diameter pillars surrounded with  ${}^6\text{LiF}$ .

The zero LLD condition is the highest possible efficiency, ranging from 41.1% for 175- $\mu\text{m}$ -deep etch to 80.8% for 650- $\mu\text{m}$ -tall pillars. Fig. 24 shows the calculated intrinsic thermal-neutron detection efficiencies as a function of LLD setting where the unit cell is 60- $\mu\text{m}$  wide and the pillars are 42- $\mu\text{m}$  wide (i.e.  $D/W_{cell} = 0.7$ ). With an LLD setting of 0 keV, the intrinsic detection efficiency is maximized at 32.2% for the 175- $\mu\text{m}$ -deep perforations and 61.6% intrinsic detection efficiency for the 650- $\mu\text{m}$ -tall pillars. Finally, Fig. 25 depicts the calculated intrinsic thermal-neutron detection efficiencies as a function of LLD setting where the unit cell is 100- $\mu\text{m}$  wide and the pillars are 70  $\mu\text{m}$  in diameter (i.e.  $D/W_{cell} = 0.7$ ). The intrinsic detection efficiency for these devices ranges from 25.7% for perforations etched to 175  $\mu\text{m}$  and 47.7% for pillars 650- $\mu\text{m}$  tall.

#### 4. Opaque perforation cases

The following section will consider devices wherein the front-side pattern is directly aligned to and an inverse image of the front-side pattern on the backside of the device. In this work, opaque means no neutron free streaming paths are present for normally incident neutrons, and there is no overlap of neutron conversion material on the front- and back-side. Three basic designs are investigated: (1) a lateral matrix of straight, parallel trenches (the “trench design”), (2) a square matrix of circular hole perforations on the front-side (the “hole design”) and circular substrate pillars on the back-side, and (3) a square matrix of circular pillars on the front-side (the “pillar design”) with

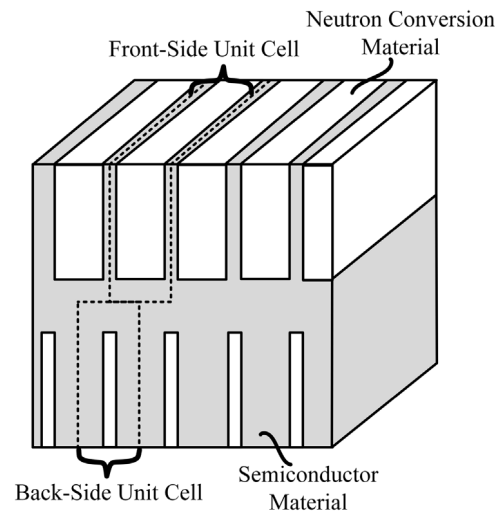


Fig. 26. The basic concept for an opaque-type straight-trenched dual-sided microstructured semiconductor neutron detector (DS-MSND). Top-side and back-side unit-cells are identical in width but are off-set. The trench dimensions are such that total device opacity is achieved, but no overlapping occurs.

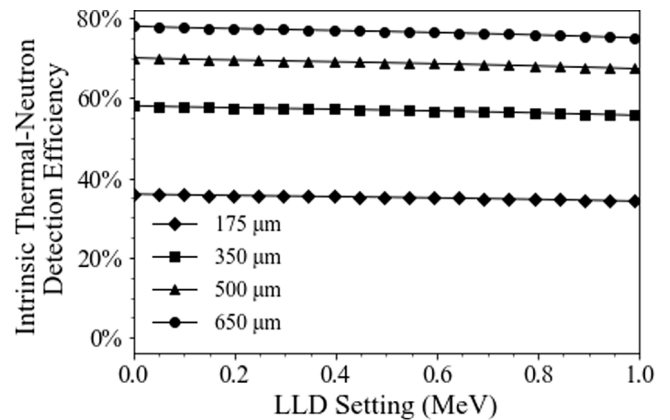


Fig. 27. Plotted are intrinsic thermal-neutron detection efficiencies for various perforation depths for the opaque straight-trench design with 20- $\mu\text{m}$  wide unit cell and 10- $\mu\text{m}$  wide trenches backfilled with  ${}^6\text{LiF}$ .

back-side circular-hole pattern. The back-side pattern for trench-type designs will involve trenches with width  $W_{cell} - T$ , as shown in Fig. 26. Hole-type patterns will involve circular holes in the top-side of the semiconductor substrate, and pillars (aligned concentrically with the holes) on the back-side of the semiconductor, as seen in Fig. 28. The pillar-type pattern is the inverse, with pillars on the top-side and holes on the back-side. The benefit of these patterns is that over absorption of incident neutrons is limited, wherein the top-side pattern overshadows the back-side pattern. For each design, the perforations are assumed to be fully backfilled with neutron conversion material with a packing fraction of 0.5.

##### 4.1. Straight trench-shaped perforations

The straight-trenched, opaque-type pattern utilizes aligned and off-set trenches on the front- and back-side semiconductor surfaces whose dimensions are inverse of one-another (Fig. 26). The pattern is simple to manufacture using common wet-etching techniques and allows for easy junction doping for good diode characteristics. Reaction products generated within the trenches have a good probability of depositing energy into the substrate, provided that the width of the trenches does not exceed that of the summed ranges of reaction products, as

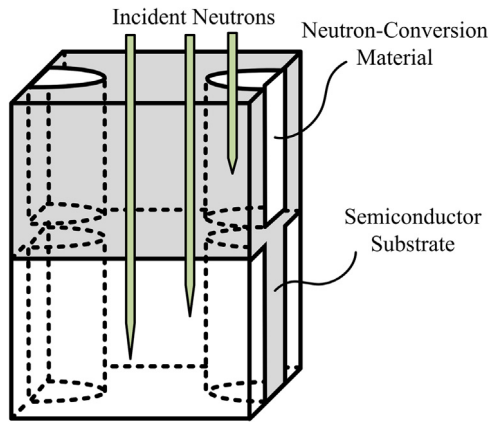


Fig. 28. Depicted is an opaque-type DS-MSND wherein the front side of the device is perforated with circular holes and the back-side is perforated with aligned circular pillars backfilled and surrounded, respectively, with neutron converting material.

depicted in Fig. 3. Here, the reaction products from the  $^{10}\text{B}(n, \alpha)^7\text{Li}$  or  $^6\text{Li}(n, t)^4\text{He}$  reactions can be emitted in any number of directions. Fig. 3 shows the notable directions: (1) along the length of the trenches where no energy will be deposited into the semiconductor and fail to produce a ‘count’, (2) along the height of the trenches where no energy will be deposited into the semiconductor and fail to produce a ‘count’, (3) where one or both reaction products are fully stopped in the semiconductor medium, likely producing a ‘count’, (4) where one or both reaction products can traverse the semiconductor into another absorber, depositing little energy into the substrate, possibly producing a ‘count’, and (5) where similar reactions can occur in the back-side trenches. Cases (3), (4), and (5) are preferred.

#### 4.1.1. Efficiencies of $^{10}\text{B}$ -filled trenches

The calculated intrinsic thermal-neutron detection efficiencies of the  $^{10}\text{B}$ -filled straight-trenched DS-MSNDs for an LLD setting of 300 keV are given in Table 8. From Table 8, there is a general trend in the detection efficiency for a given trench depth and cell width. As the ratio of the trench width to the cell width increases, the intrinsic thermal-neutron detection efficiency increases rapidly, primarily due to the increase in possible charge-particle reaction product energy deposition into the back-side fins. The back-side trenches start off much wider than the front-side trenches, resulting in greater neutron absorption efficiency, however, the thin fins are not conducive to good reaction product energy deposition. With improved energy deposition in the back-side fins, the detection efficiency rises. The optimized trench dimensions for the opaque-type design has a wider range than the off-set style of DS-MSNDs due to the complementary nature of the front- and back-side fins. Good detection efficiency is found for trench-to-unit-cell ratios of 0.3–0.8, generally. The calculated efficiencies for the opaque-type straight trench patterns as a function of LLD were not re-plotted, as the 0.50-ratio trench-width to unit-cell width is identical to the off-set type pattern, whose results can be found in Figs. 4–6.

#### 4.1.2. Efficiencies of $^6\text{LiF}$ -filled trenches

The calculated intrinsic thermal-neutron detection efficiencies of the  $^6\text{LiF}$ -filled straight-trenched DS-MSNDs for an LLD setting of 300 keV are given in Table 9. Similar to the results from the previous section, there is a trend of increasing intrinsic thermal-neutron detection efficiency with increasing  $T/W_{\text{Cell}}$  and a wide range of optimized dimensions stretching from 0.2–0.8. A maximum theoretical detection efficiency of 77.1% is apparent with a unit cell of 20  $\mu\text{m}$  and a trench-to-unit cell ratio of 0.5 for 650- $\mu\text{m}$  deep trenches. Shown in Fig. 27 are the calculated intrinsic thermal-neutron detection efficiencies as a function of LLD setting where the unit cell is 20- $\mu\text{m}$  wide and the trenches are

Table 8

Efficiencies for opaque straight trenches, with top-side width  $T$  (and back-side width  $W_{\text{Cell}} - T$ ) and depth  $H$  filled with  $^{10}\text{B}$  in a unit cell of width  $W_{\text{Cell}}$ . Neutrons are incident normally on the detector surface and the LLD cutoff energy is 300 keV.

T/ $W_{\text{Cell}}$	Cell width $W_{\text{Cell}}$ ( $\mu\text{m}$ )				
	4	6	8	10	12
Opaque dual-sided MSND, straight trench, 10-B					
Trench depth $H = 20 \mu\text{m}$					
0.10	19.7%	17.7%	17.2%	17.3%	17.6%
0.20	31.6%	28.9%	26.1%	23.4%	20.8%
0.30	32.7%	30.2%	27.8%	25.5%	23.2%
0.40	33.3%	31.1%	28.8%	26.8%	24.7%
0.50	33.5%	31.4%	29.3%	27.3%	25.4%
0.60	33.5%	31.3%	29.1%	27.0%	25.0%
0.70	33.0%	30.7%	28.3%	26.0%	23.8%
0.80	32.1%	29.6%	26.9%	24.2%	21.6%
0.90	21.0%	18.9%	18.4%	18.4%	18.7%
Trench depth $H = 40 \mu\text{m}$					
0.10	30.6%	27.1%	26.2%	26.4%	26.9%
0.20	51.1%	46.4%	41.6%	36.9%	32.3%
0.30	52.8%	48.6%	44.6%	40.6%	36.6%
0.40	53.8%	50.1%	46.5%	42.8%	39.3%
0.50	54.3%	50.7%	47.2%	43.8%	40.4%
0.60	54.2%	50.5%	46.9%	43.3%	39.9%
0.70	53.4%	49.5%	45.5%	41.5%	37.7%
0.80	52.1%	47.6%	43.0%	38.4%	33.9%
0.90	32.9%	29.2%	28.3%	28.4%	28.9%
Trench depth $H = 60 \mu\text{m}$					
0.10	37.3%	32.8%	31.8%	32.0%	32.6%
0.20	63.1%	57.2%	51.2%	45.2%	39.4%
0.30	65.2%	60.0%	54.9%	49.8%	44.8%
0.40	66.5%	61.8%	57.2%	52.7%	48.2%
0.50	67.1%	62.6%	58.2%	53.9%	49.6%
0.60	66.9%	62.4%	57.8%	53.3%	49.0%
0.70	66.0%	61.1%	56.1%	51.1%	46.2%
0.80	64.4%	58.7%	53.0%	47.1%	41.5%
0.90	40.3%	35.6%	34.5%	34.6%	35.1%
Trench depth $H = 80 \mu\text{m}$					
0.10	41.5%	36.4%	35.3%	35.5%	36.1%
0.20	70.5%	63.8%	57.1%	50.3%	43.9%
0.30	72.9%	67.0%	61.3%	55.5%	49.9%
0.40	74.3%	69.1%	63.9%	58.8%	53.8%
0.50	75.0%	70.0%	65.0%	60.2%	55.3%
0.60	74.8%	69.7%	64.6%	59.6%	54.6%
0.70	73.8%	68.3%	62.7%	57.0%	51.5%
0.80	72.0%	65.6%	59.1%	52.5%	46.1%
0.90	44.8%	39.6%	38.3%	38.4%	39.0%

10- $\mu\text{m}$  wide (i.e.  $T/W_{\text{cell}} = 0.5$ ). A maximum detection efficiency of 36.0% is calculated for trench depths of 175  $\mu\text{m}$  and zero LLD, while the maximum detection efficiency of the 650- $\mu\text{m}$  deep case is 78.0%. The intrinsic thermal-neutron detection efficiency as a function of LLD for a 60- $\mu\text{m}$  wide unit cell with 30- $\mu\text{m}$  wide trenches and 100- $\mu\text{m}$  wide unit cells with 50- $\mu\text{m}$  wide trenches are shown in Fig. 8 and Fig. 9, respectively, where they are identical to the offset design with a 0.5 trench width to pitch ratio.

#### 4.2. Circular hole-shaped perforations

Circular-hole-shaped opaque DS-MSNDs represent devices that have a circular hole etched into the front-side of the semiconductor substrate and have a semiconductor pillar reflected for the back-side structure which are backfilled and surrounded, respectively, with neutron conversion material. Devices using these perforations can be fabricated using standard ICP-RIE etching techniques, and do not require alignment to specific crystal faces for etching. Proper alignment of the two patterns will result in a device that is entirely opaque to normally incident thermal neutrons, similar to an opaque straight-trench pattern device and will result in a unit cell such as the one depicted in Fig. 28. This is different from the off-set pattern wherein neutrons may still

**Table 9**

Efficiencies for opaque straight trenches, with top-side width  $T$  (and back-side width  $W_{\text{cell}} - T$ ) and depth  $H$  filled with  $^6\text{LiF}$  in a unit cell of width  $W_{\text{cell}}$ . Neutrons are incident normally on the detector surface and the LLD cutoff energy is 300 keV.

Opaque dual-sided MSND, straight trench, 6-LiF					
T/W_Cell	Cell width $W_{\text{Cell}}$ ( $\mu\text{m}$ )				
	20	40	60	80	100
Trench depth $H = 175 \mu\text{m}$					
0.10	30.5%	24.9%	24.5%	20.7%	17.8%
0.20	34.3%	30.6%	27.1%	23.6%	20.5%
0.30	35.0%	31.7%	28.6%	25.6%	22.7%
0.40	35.4%	32.4%	29.6%	26.9%	24.3%
0.50	35.5%	32.6%	30.0%	27.5%	24.9%
0.60	35.4%	32.5%	29.8%	27.2%	24.6%
0.70	35.1%	32.0%	29.0%	26.1%	23.2%
0.80	34.5%	31.0%	27.6%	24.2%	21.2%
0.90	31.0%	25.5%	25.2%	21.6%	18.7%
Trench depth $H = 350 \mu\text{m}$					
0.10	49.1%	39.5%	38.7%	32.2%	27.1%
0.20	55.4%	49.2%	43.1%	37.1%	31.9%
0.30	56.5%	51.1%	45.9%	40.8%	35.7%
0.40	57.1%	52.2%	47.6%	43.0%	38.5%
0.50	57.4%	52.8%	48.3%	43.9%	39.7%
0.60	57.3%	52.6%	48.0%	43.5%	39.1%
0.70	56.8%	51.7%	46.7%	41.6%	36.7%
0.80	55.9%	50.1%	44.2%	38.4%	33.3%
0.90	50.2%	40.8%	40.2%	33.8%	28.9%
Trench depth $H = 500 \mu\text{m}$					
0.10	59.2%	47.4%	46.4%	38.4%	32.2%
0.20	66.8%	59.2%	51.8%	44.4%	38.0%
0.30	68.2%	61.6%	55.2%	48.9%	42.8%
0.40	68.9%	63.0%	57.4%	51.7%	46.2%
0.50	69.3%	63.7%	58.3%	52.9%	47.6%
0.60	69.2%	63.5%	57.9%	52.4%	46.9%
0.70	68.6%	62.4%	56.3%	50.1%	44.0%
0.80	67.5%	60.4%	53.3%	46.2%	39.8%
0.90	60.7%	49.2%	48.3%	40.5%	34.5%
Trench depth $H = 650 \mu\text{m}$					
0.10	65.9%	52.6%	51.5%	42.5%	35.6%
0.20	74.3%	65.9%	57.5%	49.3%	42.1%
0.30	75.9%	68.5%	61.4%	54.4%	47.4%
0.40	76.7%	70.1%	63.8%	57.5%	51.3%
0.50	77.1%	70.9%	64.8%	58.8%	52.9%
0.60	77.0%	70.7%	64.4%	58.2%	52.0%
0.70	76.4%	69.4%	62.6%	55.7%	48.8%
0.80	75.3%	67.3%	59.2%	51.3%	44.1%
0.90	67.7%	54.7%	53.7%	45.0%	38.2%

stream through the device without intersecting conversion material (Figs. 10, 18). Diffusion and contact formation can be challenging for small, high-aspect ratio features on either side of the device. The pattern benefits from excellent reaction-product detection efficiency for holes with a diameter less than the combined ranges of the reaction products but is somewhat off-set by the lack of reaction-product detection efficiency of the back-side pillars.

#### 4.2.1. Efficiencies of $^{10}\text{B}$ -filled holes

The calculated intrinsic thermal-neutron detection efficiencies of the  $^{10}\text{B}$ -filled circular-holes etched into the front-side and pillars in the back-side DS-MSND with an LLD setting of 300 keV are given in Table 10. There is a general trend of increasing detection efficiency for an increasing  $D/W_{\text{Cell}}$  ratio. As the ratio of the hole diameter,  $D$ , to the cell width,  $W_{\text{Cell}}$ , increases, the neutron absorption efficiency of the device increases on the hole side of the device and the reaction product escape probability increases on the pillar-side of the device, overall leading to a general rise in detection efficiency.

Shown in Fig. 29 are the calculated intrinsic thermal-neutron detection efficiencies as a function of LLD setting where the unit cell is  $4\text{-}\mu\text{m}$  wide and the front-side holes and back-side pillars have a diameter of  $2.8 \mu\text{m}$  (i.e.  $D/W_{\text{cell}} = 0.7$ ). The zero LLD condition gives

**Table 10**

Efficiencies for opaque circular patterns, with front-side hole diameter  $D$  and back-side pillar diameter  $D$  to depth  $H$  filled with  $^{10}\text{B}$  in a unit cell of width  $W_{\text{cell}}$ . Neutrons are incident normally on the front-side of the detector surface, and the LLD cutoff energy is 300 keV.

Opaque dual-sided MSND, front-side circular hole, 10-B					
D/W_Cell	Cell width $W_{\text{Cell}}$ ( $\mu\text{m}$ )				
	4	6	8	10	12
Trench depth $H = 20 \mu\text{m}$					
0.10	5.2%	5.3%	5.4%	5.6%	5.9%
0.20	8.3%	9.6%	9.9%	9.5%	9.0%
0.30	15.9%	15.5%	14.1%	13.0%	12.1%
0.40	23.4%	20.4%	18.4%	16.7%	15.5%
0.50	28.5%	24.9%	22.6%	20.6%	19.1%
0.60	32.1%	28.8%	26.5%	24.5%	22.7%
0.70	34.5%	32.1%	29.8%	27.9%	25.9%
0.80	35.9%	34.2%	32.3%	30.5%	28.1%
0.90	35.7%	33.5%	31.9%	30.9%	28.6%
Trench depth $H = 40 \mu\text{m}$					
0.10	5.4%	5.6%	6.0%	6.3%	6.8%
0.20	10.8%	13.1%	13.6%	12.9%	12.1%
0.30	24.0%	23.3%	21.0%	19.0%	17.5%
0.40	36.8%	31.8%	28.3%	25.5%	23.5%
0.50	45.7%	39.5%	35.5%	32.2%	29.7%
0.60	51.9%	46.3%	42.3%	38.9%	35.8%
0.70	56.0%	51.9%	48.1%	44.8%	41.3%
0.80	58.3%	55.6%	52.4%	49.3%	45.1%
0.90	58.1%	54.5%	51.7%	50.0%	45.7%
Trench depth $H = 60 \mu\text{m}$					
0.10	5.6%	5.8%	6.3%	6.6%	7.3%
0.20	12.4%	15.3%	16.0%	15.0%	14.0%
0.30	29.0%	28.1%	25.2%	22.8%	20.8%
0.40	45.1%	38.8%	34.4%	30.9%	28.3%
0.50	56.3%	48.5%	43.5%	39.4%	36.2%
0.60	64.1%	57.1%	52.0%	47.8%	43.9%
0.70	69.3%	64.1%	59.4%	55.2%	50.8%
0.80	72.1%	68.7%	64.7%	60.8%	55.5%
0.90	71.8%	67.4%	63.9%	61.6%	56.4%
Trench depth $H = 80 \mu\text{m}$					
0.10	5.7%	6.0%	6.5%	6.9%	7.6%
0.20	13.4%	16.7%	17.4%	16.3%	15.2%
0.30	32.1%	31.1%	27.9%	25.1%	22.9%
0.40	50.3%	43.1%	38.2%	34.3%	31.3%
0.50	62.9%	54.1%	48.4%	43.8%	40.2%
0.60	71.6%	63.7%	58.0%	53.3%	48.9%
0.70	77.5%	71.7%	66.3%	61.6%	56.7%
0.80	80.6%	76.8%	72.3%	67.9%	62.0%
0.90	80.4%	75.4%	71.5%	68.9%	63.0%

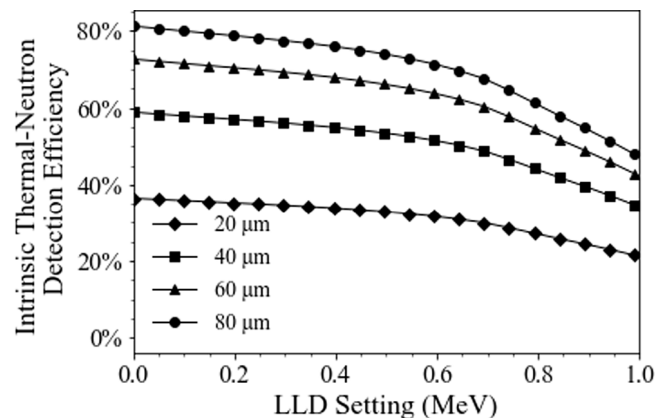
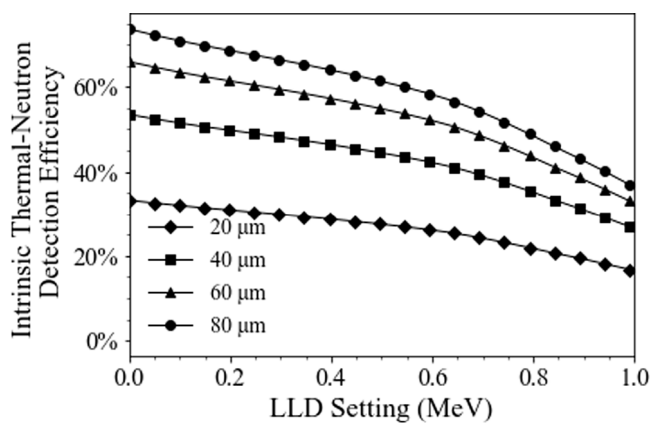


Fig. 29. Plotted are intrinsic thermal-neutron detection efficiencies for various perforation depths for the front-side circular-hole, back-side pillar design with  $4 \mu\text{m}$  unit cell and  $2.8 \mu\text{m}$  diameter features with  $^{10}\text{B}$  converter.

**Table 11**

Efficiencies for opaque circular patterns, with front-side hole diameter  $D$  and back-side pillar diameter  $D$  to depth  $H$  filled with  ${}^6\text{LiF}$  in a unit cell of width  $W_{\text{cell}}$ . Neutrons are incident normally on the front detector surface, and the LLD cutoff energy is 300 keV.

Opaque dual-sided MSND, front-side circular hole, 6-LiF					
D/ $W_{\text{Cell}}$	Cell width $W_{\text{Cell}}$ ( $\mu\text{m}$ )				
	20	40	60	80	100
Trench depth $H = 175 \mu\text{m}$					
0.10	6.1%	6.2%	6.7%	6.6%	6.3%
0.20	12.1%	12.5%	10.9%	9.7%	8.9%
0.30	22.0%	17.9%	15.0%	13.2%	11.9%
0.40	29.1%	22.8%	19.2%	17.0%	15.4%
0.50	32.8%	27.2%	23.4%	20.9%	18.9%
0.60	35.0%	31.0%	27.3%	24.7%	22.5%
0.70	36.5%	33.7%	30.6%	28.1%	25.5%
0.80	37.2%	35.4%	33.0%	30.7%	27.5%
0.90	37.5%	35.7%	34.2%	31.6%	28.1%
Trench depth $H = 350 \mu\text{m}$					
0.10	7.2%	7.6%	8.3%	8.1%	7.6%
0.20	17.7%	18.4%	15.5%	13.6%	12.1%
0.30	34.6%	27.4%	22.6%	19.6%	17.4%
0.40	46.7%	35.8%	29.9%	26.0%	23.2%
0.50	52.9%	43.4%	37.0%	32.7%	29.4%
0.60	56.6%	49.9%	43.8%	39.3%	35.5%
0.70	59.0%	54.6%	49.4%	45.2%	40.6%
0.80	60.3%	57.4%	53.5%	49.5%	43.9%
0.90	60.8%	57.9%	55.6%	51.0%	45.0%
Trench depth $H = 500 \mu\text{m}$					
0.10	7.8%	8.3%	9.2%	9.0%	8.4%
0.20	20.8%	21.5%	18.1%	15.6%	13.9%
0.30	41.5%	32.7%	26.7%	23.0%	20.3%
0.40	56.2%	42.9%	35.6%	30.9%	27.5%
0.50	63.9%	52.2%	44.4%	39.2%	35.1%
0.60	68.3%	60.2%	52.7%	47.2%	42.5%
0.70	71.3%	65.9%	59.6%	54.4%	48.8%
0.80	72.8%	69.4%	64.7%	59.6%	52.8%
0.90	73.4%	70.0%	67.1%	61.4%	54.1%
Trench depth $H = 650 \mu\text{m}$					
0.10	8.3%	8.8%	9.8%	9.5%	8.8%
0.20	22.8%	23.6%	19.7%	17.0%	15.1%
0.30	46.1%	36.2%	29.4%	25.3%	22.2%
0.40	62.6%	47.6%	39.5%	34.1%	30.4%
0.50	71.1%	58.0%	49.3%	43.4%	38.9%
0.60	76.1%	66.9%	58.6%	52.4%	47.2%
0.70	79.4%	73.4%	66.4%	60.5%	54.2%
0.80	81.1%	77.2%	71.9%	66.4%	58.7%
0.90	81.8%	78.0%	74.7%	68.3%	60.1%



**Fig. 30.** Plotted are intrinsic thermal-neutron detection efficiencies for various perforation depths for the front-side circular-hole, back-side pillar design with 8  $\mu\text{m}$  unit cell and 5.6  $\mu\text{m}$  diameter features with  ${}^{10}\text{B}$  converter.

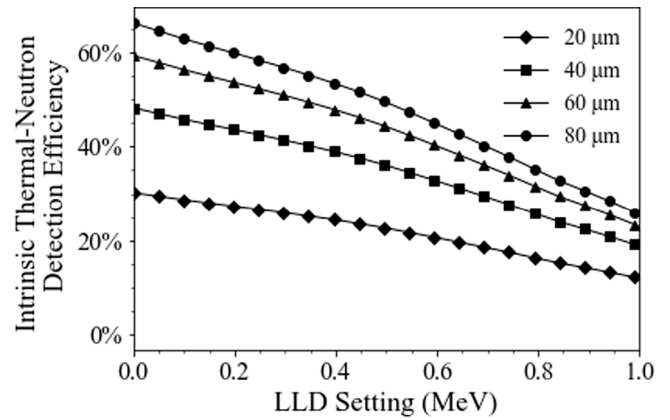


**Fig. 31.** Plotted are intrinsic thermal-neutron detection efficiencies for various perforation depths for the front-side circular-hole, back-side pillar design with 12  $\mu\text{m}$  unit cell and 8.4  $\mu\text{m}$  diameter features with  ${}^{10}\text{B}$  converter.

the highest possible detection efficiency, ranging from 36.4% for 20- $\mu\text{m}$ -deep trenches to 81.3% for 60- $\mu\text{m}$ -deep holes. Fig. 30 shows the calculated intrinsic thermal-neutron detection efficiencies as a function of LLD setting where the unit cell is 8- $\mu\text{m}$  wide and the front-side holes and the back-side pillars are 5.6- $\mu\text{m}$  wide (i.e.  $D/W_{\text{cell}} = 0.7$ ). With an LLD setting of 0 keV, the intrinsic detection efficiency is maximized at 33.2% for the 20- $\mu\text{m}$ -deep holes and 73.6% intrinsic efficiency for the 80- $\mu\text{m}$ -deep holes. Finally, Fig. 31 depicts the calculated intrinsic thermal-neutron detection efficiencies as a function of LLD setting where the unit cell is 12- $\mu\text{m}$  wide and the front-side holes and back-side pillars are 8.4  $\mu\text{m}$  in diameter (i.e.  $D/W_{\text{cell}} = 0.7$ ). The intrinsic detection efficiency for these devices ranges from 30.2% for 20- $\mu\text{m}$ -deep perforations and 66.2% for 80- $\mu\text{m}$ -deep perforations. The reducing detection efficiency as a function of unit cell width at the 0 keV level is indicative of the decreasing charged-particle reaction product escape solid angle within the neutron conversion material.

#### 4.2.2. Efficiencies of ${}^6\text{LiF}$ -filled holes

The calculated intrinsic thermal-neutron detection efficiencies of  ${}^6\text{LiF}$ -filled DS-MSNDs etched with front-side circular holes and back-side circular pillars with LLD setting of 300 keV are given in Table 11. Like the previous section, as the ratio of the hole diameter to the cell width increases, the neutron absorption efficiency of the front-side holes and the reaction product detection efficiency in the backside pillars increases culminating in a general increase in detection efficiency. The optimal detection efficiency occurs for a hole-to-cell-width ratio of 0.9 for a 20- $\mu\text{m}$  wide unit.

Shown in Fig. 32 are the calculated intrinsic thermal-neutron detection efficiencies as a function of LLD setting where the unit cell is 20- $\mu\text{m}$  wide and the front-side holes have a diameter of 14  $\mu\text{m}$  (i.e.  $D/W_{\text{cell}} = 0.7$ ). The zero LLD condition is the highest possible efficiency, ranging from 36.9% for 175- $\mu\text{m}$ -deep holes to 80.2% for 650- $\mu\text{m}$ -deep holes. Fig. 33 shows the calculated intrinsic thermal-neutron detection efficiencies as a function of LLD setting where the unit cell is 60- $\mu\text{m}$  wide and the holes are 42- $\mu\text{m}$  wide (i.e.  $D/W_{\text{cell}} = 0.7$ ). With an LLD setting of 0 keV, the intrinsic detection efficiency is maximized at 31.6% for the 175- $\mu\text{m}$ -deep holes and 68.3% intrinsic efficiency for the 650- $\mu\text{m}$ -deep holes. Finally, Fig. 34 depicts the calculated intrinsic thermal-neutron detection efficiencies as a function of LLD setting where the unit cell is 100- $\mu\text{m}$  wide and the holes are 70  $\mu\text{m}$  in diameter (i.e.  $D/W_{\text{cell}} = 0.7$ ). The intrinsic detection efficiency for these devices ranges from 27.0% for holes etched to 175  $\mu\text{m}$  and 57.2% for holes etched to 650  $\mu\text{m}$ .

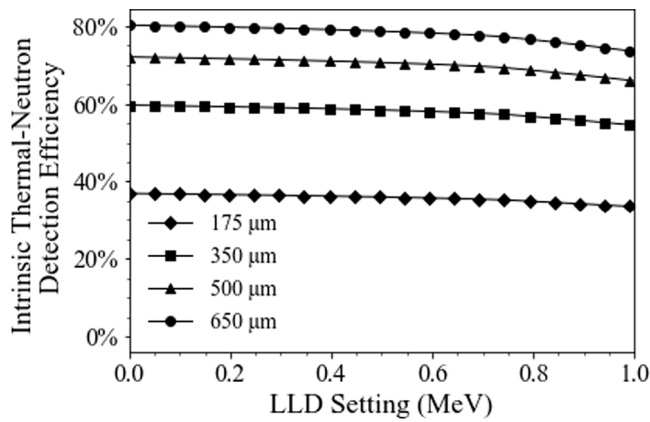


Fig. 32. Plotted are intrinsic thermal-neutron detection efficiencies for various perforation depths for the front-side circular-hole, back-side pillar design with 20- $\mu\text{m}$  unit cell and 14- $\mu\text{m}$  diameter with  $^6\text{LiF}$  converter.

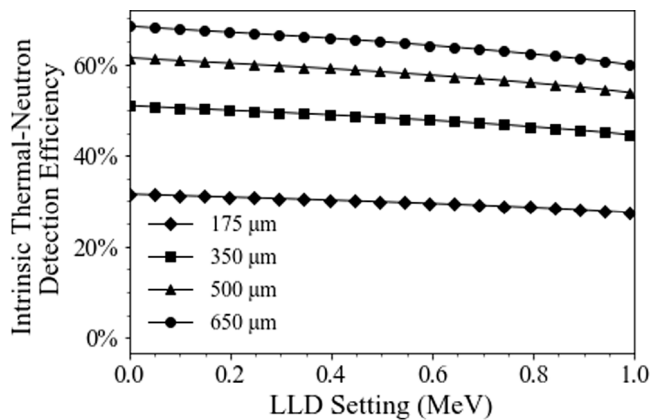


Fig. 33. Plotted are intrinsic thermal-neutron detection efficiencies for various perforation depths for the front-side circular-hole, back-side pillar design with 60- $\mu\text{m}$  unit cell and 42- $\mu\text{m}$  diameter with  $^6\text{LiF}$  converter.

### 4.3. Circular pillar-shaped structures

The simulations in this section cover opaque-type patterned DS-MSNDs having front-side circular pillars and back-side circular holes. The pattern is the same as show in Fig. 28, but the neutrons are incident on the pillar side of the device. Again, the opaque design eliminates any neutron free streaming paths that would be present in an offset-type patterned DS-MSNDs. The circular perforations can be formed using RIE techniques. Contact formation on small features found on either end of the  $D/W_{cell}$  limits can be challenging and cause problems with dead regions due to dopant diffusion in the material. The results of the simulation are very similar to those results for the opaque pattern with front-side circular holes with the intrinsic detection efficiency slightly increased. The small differences are likely caused by a decreased probability of reaction products escaping the device on the pillar side without first interacting in the silicon features at the surface of the DS-MSND.

#### 4.3.1. Efficiencies of $^{10}\text{B}$ -filled-surrounded pillars

The results for the simulations are displayed in Table 12 where the LLD was set at 300 keV to determine the intrinsic-thermal neutron detection efficiency. As seen in the previous section, the intrinsic thermal-neutron detection efficiency increased as the feature diameter to unit cell width,  $D/W_{cell}$ , increased to 0.9 with the maximum detecting efficiency predicted to be 81% for 80- $\mu\text{m}$  deep features on a 20- $\mu\text{m}$  wide pitch. On the pillar side of the DS-MSND, the reaction product escape probability from the neutron conversion material into the silicon

Table 12

Efficiencies for opaque circular patterns, with front-side pillar diameter  $D$  and back-side hole diameter  $D$  to depth  $H$  filled with  $^{10}\text{B}$  in a unit cell of width  $W_{cell}$ . Neutrons are incident normally on the front detector surface, and the LLD cutoff energy is 300 keV.

Opaque dual-sided MSND, front-side circular pillar, 10B					
D/WCell	Unit cell width, WCell ( $\mu\text{m}$ )				
	4	6	8	10	12
Trench depth H= 20 $\mu\text{m}$					
0.10	3.6%	3.8%	4.0%	4.1%	4.4%
0.20	6.8%	8.2%	8.5%	8.1%	7.6%
0.30	14.6%	14.3%	12.9%	11.8%	10.9%
0.40	22.4%	19.4%	17.3%	15.7%	14.5%
0.50	27.8%	24.1%	21.7%	19.8%	18.3%
0.60	31.6%	28.3%	25.9%	23.9%	22.1%
0.70	34.2%	31.7%	29.5%	27.7%	25.6%
0.80	35.7%	34.1%	32.3%	30.5%	28.1%
0.90	35.9%	33.9%	32.2%	31.2%	28.9%
Trench depth H= 40 $\mu\text{m}$					
0.10	2.7%	2.9%	3.3%	3.6%	4.1%
0.20	8.2%	10.7%	11.2%	10.4%	9.6%
0.30	21.8%	21.1%	18.8%	16.8%	15.2%
0.40	35.0%	29.9%	26.3%	23.5%	21.5%
0.50	44.3%	38.0%	33.9%	30.6%	28.1%
0.60	50.9%	45.2%	41.1%	37.8%	34.7%
0.70	55.4%	51.3%	47.5%	44.2%	40.7%
0.80	58.1%	55.4%	52.2%	49.2%	45.1%
0.90	58.5%	55.0%	52.2%	50.4%	46.4%
Trench depth H= 60 $\mu\text{m}$					
0.10	2.0%	2.3%	2.8%	3.2%	3.9%
0.20	9.0%	12.1%	12.8%	11.8%	10.8%
0.30	26.1%	25.3%	22.4%	19.8%	17.9%
0.40	42.9%	36.4%	31.9%	28.4%	25.7%
0.50	54.6%	46.6%	41.5%	37.3%	34.1%
0.60	62.9%	55.7%	50.6%	46.3%	42.3%
0.70	68.5%	63.4%	58.6%	54.5%	50.1%
0.80	71.9%	68.5%	64.6%	60.7%	55.5%
0.90	72.4%	68.1%	64.6%	62.4%	57.2%
Trench depth H= 80 $\mu\text{m}$					
0.10	1.7%	2.0%	2.6%	3.0%	3.7%
0.20	9.6%	13.1%	13.8%	12.7%	11.5%
0.30	28.9%	27.9%	24.6%	21.7%	19.5%
0.40	47.7%	40.4%	35.4%	31.4%	28.4%
0.50	60.9%	51.9%	46.1%	41.5%	37.8%
0.60	70.3%	62.2%	56.4%	51.6%	47.1%
0.70	76.6%	70.8%	65.4%	60.8%	55.8%
0.80	80.4%	76.7%	72.2%	67.9%	62.0%
0.90	81.0%	76.2%	72.3%	69.7%	63.9%

pillars improves as the diameter of the silicon pillars increases, and on the hole-side of the DS-MSND, the absorption probability is maximized as the hole diameter increases.

The maximum possible detection efficiency corresponding to an LLD setting of zero is shown for opaque-type pillar DS-MSNDs with a 4  $\mu\text{m}$  unit cell and feature diameter to cell width,  $D/W_{cell}$ , ratio of 0.7 is shown in Fig. 35. The maximum detection efficiency is 36.2% for 20- $\mu\text{m}$  tall pillars and 80.6% for 80- $\mu\text{m}$  tall pillars. Fig. 36 shows the intrinsic thermal-neutron detection efficiency as a function of LLD for front-side pillar opaque DS-MSNDs with a unit cell width of 8  $\mu\text{m}$  and feature diameter of 5.6 ( $D/W_{cell} = 0.7$ ). The zero-LLD detection efficiency ranges from 32.9% to 72.6% for 20- $\mu\text{m}$ -tall and 80- $\mu\text{m}$ -tall pillars, respectively. Finally, the detection efficiency for front-side opaque pillar DS-MSNDs with  $^{10}\text{B}$  conversion material, 12- $\mu\text{m}$  wide unit cells and 8.4- $\mu\text{m}$  diameter features are plotted in Fig. 37. The intrinsic maximum intrinsic-thermal neutron detection efficiency for 20- $\mu\text{m}$  deep features was 29.8%, and at 0 keV LLD the detection efficiency for 80- $\mu\text{m}$  deep feature was 65%.

**Table 13**

Efficiencies for opaque circular patterns, with front-side pillar diameter  $D$  and back-side hole diameter  $D$  to depth  $H$  filled with  ${}^6\text{LiF}$  in a unit cell of width  $W_{\text{cell}}$ . Neutrons are incident normally on the front detector surface, and the LLD cutoff energy is 300 keV.

Opaque dual-sided MSND, front-side circular pillar, ${}^6\text{LiF}$					
D/WCell	Unit cell width, WCell ( $\mu\text{m}$ )				
	20	40	60	80	100
Trench depth $H = 175 \mu\text{m}$					
0.10	4.7%	4.9%	5.3%	5.2%	4.9%
0.20	10.9%	11.4%	9.7%	8.5%	7.7%
0.30	21.1%	16.8%	14.0%	12.1%	10.8%
0.40	28.5%	21.9%	18.4%	16.0%	14.4%
0.50	32.4%	26.5%	22.8%	20.1%	18.2%
0.60	34.7%	30.6%	26.9%	24.2%	21.9%
0.70	36.3%	33.5%	30.5%	27.9%	25.2%
0.80	37.2%	35.3%	33.0%	30.7%	27.5%
0.90	37.5%	35.8%	34.5%	31.8%	28.4%
Trench depth $H = 350 \mu\text{m}$					
0.10	4.8%	5.1%	5.9%	5.6%	5.2%
0.20	15.6%	16.2%	13.3%	11.2%	9.8%
0.30	33.0%	25.6%	20.6%	17.4%	15.2%
0.40	45.5%	34.3%	28.1%	24.1%	21.4%
0.50	52.2%	42.2%	35.7%	31.1%	27.9%
0.60	56.1%	49.1%	42.8%	38.2%	34.3%
0.70	58.7%	54.1%	48.9%	44.6%	40.0%
0.80	60.2%	57.3%	53.4%	49.4%	44.0%
0.90	60.9%	58.2%	55.8%	51.4%	45.6%
Trench depth $H = 500 \mu\text{m}$					
0.10	4.8%	5.2%	6.1%	5.8%	5.3%
0.20	18.1%	18.9%	15.2%	12.7%	11.0%
0.30	39.4%	30.3%	24.1%	20.3%	17.6%
0.40	54.7%	41.0%	33.4%	28.5%	25.1%
0.50	62.8%	50.7%	42.7%	37.2%	33.1%
0.60	67.6%	59.1%	51.4%	45.8%	41.0%
0.70	70.9%	65.3%	58.9%	53.6%	48.0%
0.80	72.7%	69.1%	64.4%	59.6%	52.9%
0.90	73.6%	70.3%	67.5%	62.0%	54.9%
Trench depth $H = 650 \mu\text{m}$					
0.10	4.8%	5.3%	6.3%	6.0%	5.3%
0.20	19.7%	20.6%	16.5%	13.6%	11.7%
0.30	43.6%	33.4%	26.5%	22.2%	19.2%
0.40	60.8%	45.4%	36.9%	31.4%	27.6%
0.50	69.9%	56.2%	47.3%	41.1%	36.6%
0.60	75.3%	65.7%	57.0%	50.9%	45.5%
0.70	78.9%	72.7%	65.5%	59.6%	53.3%
0.80	80.9%	77.0%	71.7%	66.2%	58.7%
0.90	82.0%	78.3%	75.2%	69.0%	61.0%

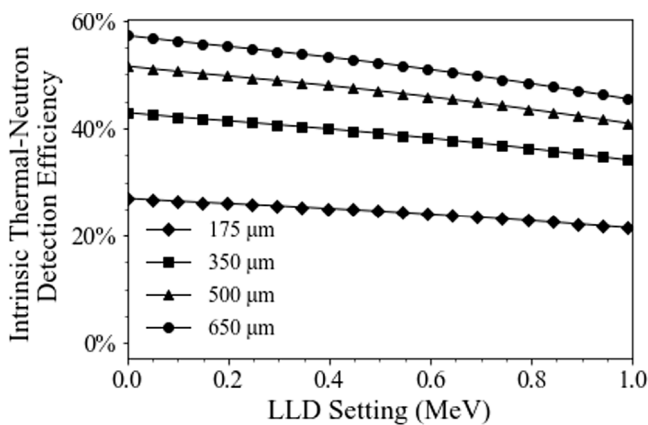


**Fig. 34.** Plotted are intrinsic thermal-neutron detection efficiencies for various perforation depths for the front-side circular-hole, back-side pillar design with 100- $\mu\text{m}$  unit cell and 70- $\mu\text{m}$  diameter features with  ${}^6\text{LiF}$  converter.

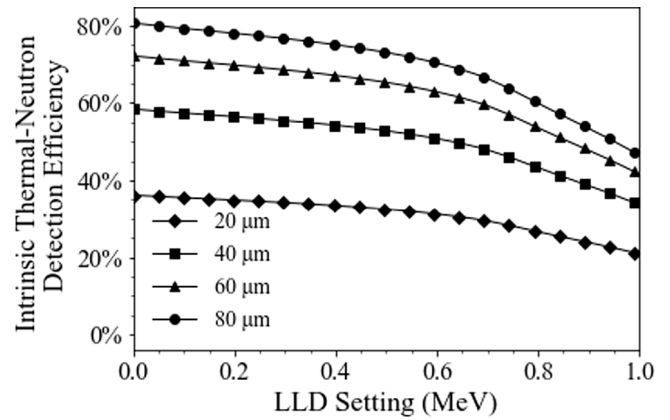


**Fig. 35.** Plotted are intrinsic thermal-neutron detection efficiencies for various perforation depths for the front-side circular-pillar, back-side hole design with 4- $\mu\text{m}$  unit cell and 2.8- $\mu\text{m}$  diameter features with  ${}^{10}\text{B}$  converter.

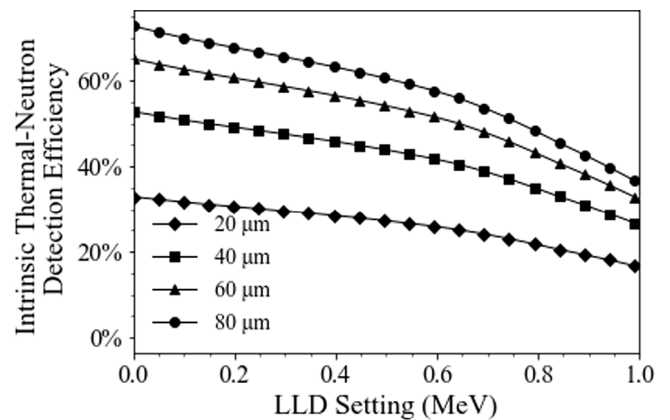


**Fig. 36.** Plotted are intrinsic thermal-neutron detection efficiencies for various perforation depths for the front-side circular-pillar, back-side hole design with 8- $\mu\text{m}$  unit cell and 5.6- $\mu\text{m}$  diameter features with  ${}^{10}\text{B}$  converter.

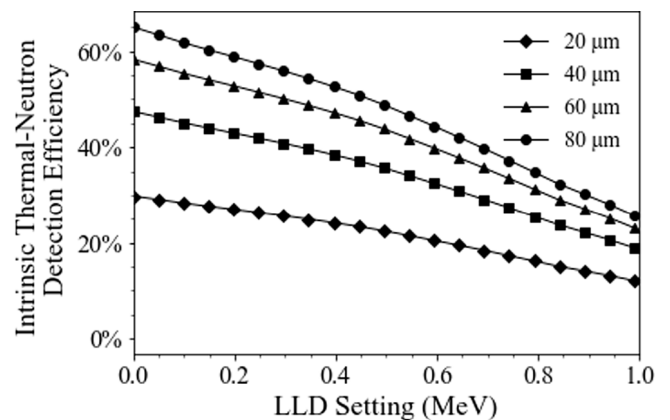


**Fig. 37.** Plotted are intrinsic thermal-neutron detection efficiencies for various perforation depths for the front-side circular-pillar, back-side hole design with 12- $\mu\text{m}$  unit cell and 8.4- $\mu\text{m}$  diameter features with  ${}^{10}\text{B}$  converter.

4.3.2. Efficiencies of  ${}^6\text{LiF}$ -surrounded pillars

DS-MSND devices with an opaque pattern comprising front-side circular pillars surrounded by  ${}^6\text{LiF}$  and back-side circular holes filled with  ${}^6\text{LiF}$  were simulated. The results of the simulations are shown in Table 13. Again, the detection efficiency tended to increase as

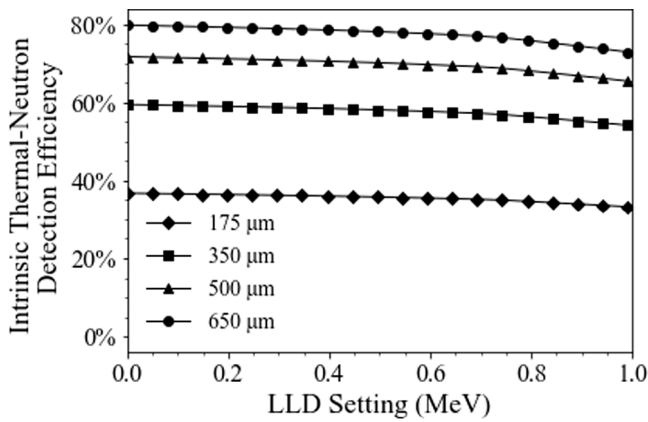


Fig. 38. Plotted are intrinsic thermal-neutron detection efficiencies for various perforation depths for the front-side circular-pillar, back-side hole design with 20-μm unit cell and 14-μm diameter features with <sup>6</sup>LiF converter.

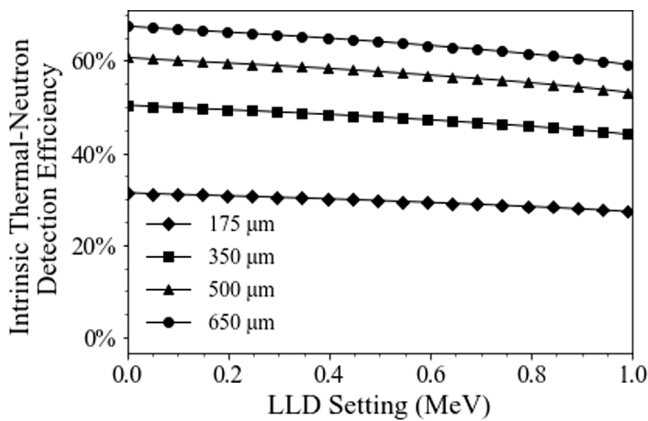


Fig. 39. Plotted are intrinsic thermal-neutron detection efficiencies for various perforation depths for the front-side circular-pillar, back-side hole design with 60-μm unit cell and 42-μm diameter features with <sup>6</sup>LiF converter.

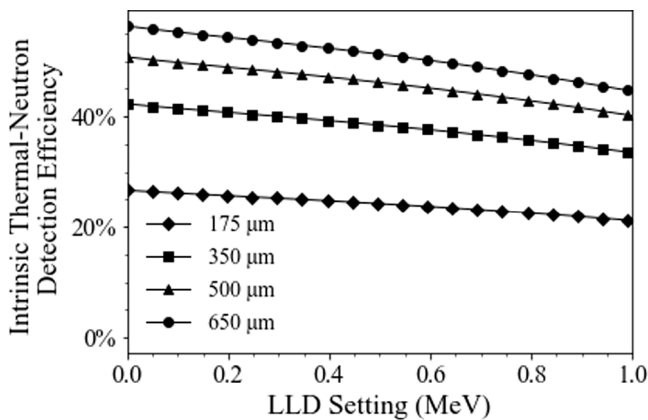


Fig. 40. Plotted are intrinsic thermal-neutron detection efficiencies for various perforation depths for the front-side circular-pillar, back-side hole design with 100-μm unit cell and 70-μm diameter features with <sup>6</sup>LiF converter.

the  $D/W_{cell}$  ratio increased with the maximum theoretical detection efficiency for this style of DS-MSND with a 300 keV LLD was 82.0%.

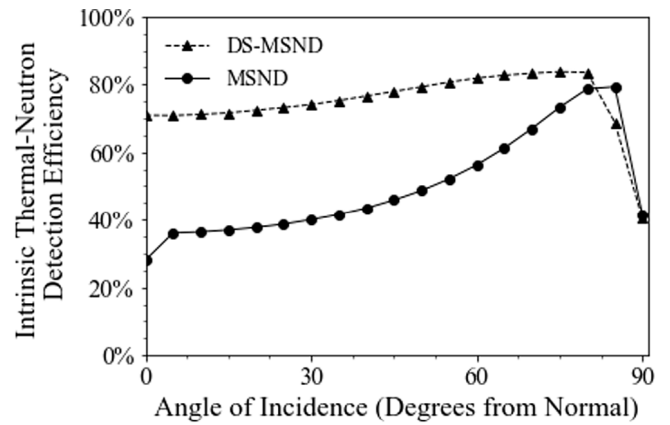


Fig. 41. Plotted is the intrinsic thermal-neutron detection efficiency for a straight-trench MSND and offset straight-trench DS-MSND with respect to increasing incident neutron angle. The MSND had 400 μm-deep trenches that were 20-μm wide with a unit-cell width of 40 μm. The trench depth for the DS-MSND was 650 μm, and all other trench dimensions were the same. Both devices were backfilled with <sup>6</sup>LiF with a packing fraction of 0.5.

The intrinsic thermal-neutron detection efficiency of the opaque DS-MSND with front-side pillars as a function of LLD setting is shown in Fig. 38 for the four microfeature depths simulated with a 20-μm wide unit cell. The maximum intrinsic thermal-neutron detection efficiency for 175-μm deep features was 36.8% and occurs at 0 keV LLD. Similarly, for 650 μm deep features 79.8% was the maximum attainable detection efficiency with no LLD. For a 60-μm wide unit cell and 42-μm diameter features, the maximum intrinsic thermal-neutron detection efficiency for 175 and 650-μm deep microstructures was 31.4% and 67.4%, respectively (see Fig. 39). The zero LLD intrinsic thermal-neutron detection efficiency for the largest unit cell simulated, 100 μm, with a 0.7  $D/W_{cell}$  ratio was 26.7% for 175-μm deep features and 56.3% for 650-μm deep features (Fig. 40).

### 5. Practical considerations

The following section pertains to real-world and other considerations that must be examined when designing and fabricating a DS-MSND device. The efficiency calculations found in prior sections were calculated for optimal conditions wherein thermal neutrons are normally incident on the front-side detector face and collection of the induced electron-hole pairs in the silicon is complete. These topics, along with issues to consider when fabricating DS-MSNDs, are discussed here.

#### 5.1. Angular considerations

All calculations in previous sections were performed using a normally-incident beam of collimated thermal neutrons. A real-world measurement for comparison and validation can be achieved through the use of a diffracted neutron beam port, such as the one found at the Kansas State University TRIGA Mk II research reactor [22]. The normally-incident thermal beam is attractive, because it is repeatable, easily accounts for room-scattered neutrons, background gamma-rays, and has no need to consider corrections for the presence of higher-energy neutrons, all of which can be more difficult to correct for in moderated <sup>252</sup>Cf test scenarios. As a side note, when DS-MSND or MSND based <sup>3</sup>He-replacement detector systems that will be utilized in mixed radiation environments containing fast neutrons, thermal neutrons, and gamma-rays are designed and deployed, higher fidelity models are required to predict and validate the detector response [27]. These models are often also used to optimize neutron moderator cask design for the detector to improve fast neutron sensitivity.

When a collimated beam of thermal neutrons deviates from normal incidence, the intrinsic detection efficiency of MSND-based technology changes significantly (Fig. 41). The change in intrinsic thermal-neutron detection efficiency is caused by the closing of the streaming paths between the trenches. In a real-world application wherein neutrons are irradiating the entire surface of the detector, the neutrons will appear collimated when the source is a sufficient distance from an unmoderated detector. As the angle of the detector changes relative to the source, the intrinsic thermal-neutron detection efficiency will change as in Fig. 41; however, as the angle increases and the detection efficiency increases, the reduction of the presented area will reduce the count rate by a factor of cosine of the detector angle. If the detector is co-located with a neutron moderator, the neutrons entering the detector will no longer appear collimated due to a high probability of scattering near the detector.

The change in intrinsic thermal-neutron detection efficiency as a function of the neutron incident angle for a DS-MSND is less dramatic, because the neutron streaming paths do not exist for neutrons entering the front (or back) surface of the detector at any angle for offset DS-MSNDs with straight trenches with  $T/W_{cell}$  greater than 0.5 and all opaque designs. The slight increase in detection efficiency at angles of incidence greater than  $0^\circ$  can be attributed an increased neutron path length in the conversion material. The drop-off in detection efficiency that occurs at high incident angles is caused by neutrons entering the side of the diode and streaming through the bulk silicon beneath the trenches or between the sets of front and back-side trenches for MSNDs and DS-MSNDs, respectively.

### 5.2. Micro-feature fabrication considerations

Higher detection efficiency is achieved with deeply-etched microstructures, thereby, increasing the intrinsic thermal-neutron absorption efficiency. Issues with deep, anisotropic etching of perforations limited the capability of early MSNDs. Dry-etching techniques like ICP-RIE requires high-forward power bias to achieve perforations up to 250- $\mu\text{m}$  deep. This high forward power often leaves damaged sidewalls and significant lateral etching. The resulting sidewall damage can be mitigated through oxidation and BOE etching, but leakage current due to high rates of surface recombination often renders such devices unusable. However, the benefit to dry plasma etching is that almost any pattern can be etched into the substrate, including straight trenches, circular holes, pillars and sinusoidal trenches. Additionally, dry etching techniques can be used to etch numerous substrate materials, including Si, SiC, etc. Wet-etching techniques like KOH etching has resulted in devices etched up to 500- $\mu\text{m}$  deep with a 100:1 vertical-to-lateral etching ratio. KOH wet etching results in smooth side walls with limited surface recombination leakage current. However, due to the nature of the etching process, patterns must be aligned to the (111) plane for Si. Straight trenches are easily fabricated in Si, however more complicated patterns have yet to be successful. Wet etching of alternative substrates like SiC and GaAs is difficult as KOH does not anisotropically etch these semiconductors. However, for Si, wet etching techniques tend to be a better choice for mass production, because the wafer throughput is limited by the size of the KOH bath. Comparatively, the throughput of dry etching processes is limited by the wafer capacity of the RIE system, which is typically significantly smaller than the wet-etching counterpart.

Recall that  $^6\text{LiF}$ -based devices required deeper-etched microfeatures compared to  $^{10}\text{B}$ -based counterparts to achieve similar intrinsic thermal-neutron detection efficiency. For  $^{10}\text{B}$ -backfilled detectors, the microfeatures could feasibly be etched with either dry or wet etching processes. Anisotropic wet etch processing is critical to facilitating the deeper microfeatures required for high-efficiency  $^6\text{LiF}$ -backfilled detectors. The pitfalls of RIE like damage to sidewalls, long etch times, and reduced throughput are mitigated by the wet etching processes.

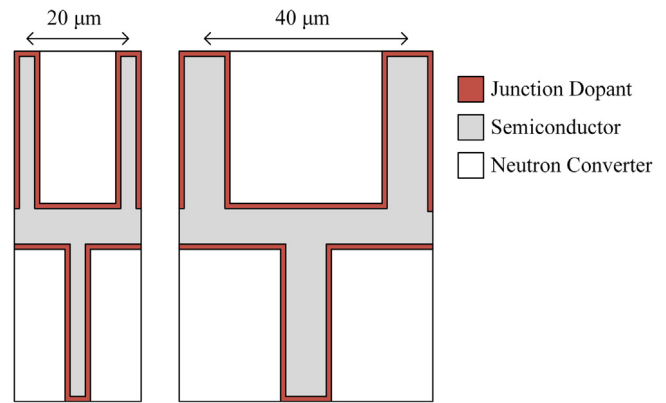


Fig. 42. Diagram depicting effect of dead regions from the junction dopant within the silicon microfeature. 20- $\mu\text{m}$  and 40- $\mu\text{m}$  wide unit cells are shown with a 0.75 trench-width to unit-cell-width ratio and a dopant diffusion depth of 1  $\mu\text{m}$ . The 40- $\mu\text{m}$  wide unit cell features a larger active-to-dead region ratio within the semiconductor volume leading to increased measurable charge deposition.

### 5.3. Junction-formation considerations

The  $pn$ -junctions on the DS-MSNDs required to drift the charge carriers can be formed through solid-source diffusion, liquid-source diffusion, or ion implantation. Ion implantation can be used if planar contacts on the tops of the micro-features are desired. However, it is challenging to form conformal junctions with ion implantation, because the micro-features shield the ion beam not allowing dopant to be implanted onto the sidewalls of the high aspect-ratio cavities. In liquid-source or solid-source diffusion conformal junctions can more readily be achieved, because the source material can diffuse as a gas down the micro-features and deposit on the semiconductor sidewall. If conformal junctions are made, the region at the edge of the micro-feature sidewall where the dopants are diffused and activated will be largely insensitive to the charge carriers created by reaction-products due to the electric field in the region. This will cause a down-shift in the spectral features of the reaction product spectrum and increase the rate at which the detection efficiency decreases as the LLD is increased. The relative magnitude of this effect on the detection efficiency is going to increase as the size of the semiconductor micro-feature decreases, because the ratio of dead region volume to the active semiconductor volume will increase (Fig. 42). This effect is more of a problem for  $^{10}\text{B}$ -backfilled DS-MSNDs than for  $^6\text{LiF}$ -backfilled DS-MSND, because the  $^{10}\text{B}$  reaction products have lower energies and therefore shorter ranges. For example, if the dopant is diffused only to a depth of 0.5  $\mu\text{m}$ , 33% of the fin would be insensitive to the reaction products for a straight-trench pattern with 6- $\mu\text{m}$  unit cell and 0.5 trench width to unit cell ratio. Thus, some of the results for simulations with small unit cells and large micro-feature width to unit cell width ratios may be practically unattainable due to fabrication limitations. Small semiconductor micro-features are also more fragile and therefore are more prone to breaking during the micro-cavity backfilling process. Damaged semiconductor micro-features will increase the leakage current of the device requiring an increased LLD which limits the detection efficiency. For these reasons, straight-trenched,  $^6\text{LiF}$ -backfilled MSNDs and DS-MSNDs are commonly fabricated with a unit-cell width of 30  $\mu\text{m}$ .

### 5.4. Signal-to-noise ratio and gamma-ray sensitivity

An additional consideration for the DS-MSND design is the signal to noise ratio for the detector. Ideally, one would be able to use simple pulse height discrimination to determine if the signal pulse was from a neutron (reaction products) or background phenomena like gamma rays or electronic noise. The background signal tends to appear

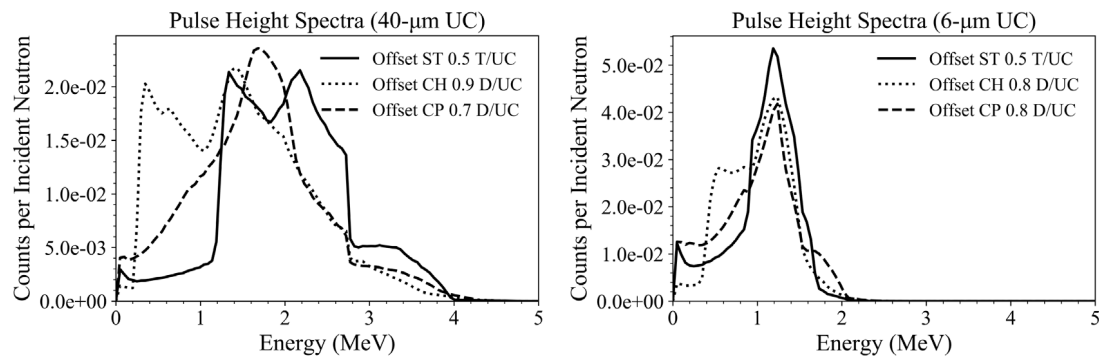


Fig. 43. (Left) Simulated pulse height spectrum for 650- $\mu\text{m}$  deep, offset Straight Trench (ST), Circular Hole (CH), and Circular Pillar (CP) DS-MSNDs with a 40- $\mu\text{m}$  unit cell and optimized microfeature width to unit cell width ratio. (Right) Simulated pulse height spectrum for 80- $\mu\text{m}$  deep,  $^{10}\text{B}$ -backfilled, offset, DS-MSNDs with a 6- $\mu\text{m}$  and optimized feature width to unit cell width ratio.

in the lower energy region of the pulse height spectrum. Therefore, an ideal reaction product spectrum would have little to no tallies in the lower energy bins such that a lower level discriminator can be set that rejects most of the background signal with only a small decrease in neutron detection efficiency. Fig. 43 shows example pulse height spectra for optimized microfeature patterns for  $^{10}\text{B}$ -backfilled and  $^6\text{LiF}$ -backfilled DS-MSNDs. The straight-trench,  $^6\text{LiF}$ -backfilled DS-MSND pulse height spectrum has the highest signal to noise ratio with the lowest valley between the background and neutron induced signal. Thus, while it may not have the highest possible detection efficiency of the designs considered, the straight-trench,  $^6\text{LiF}$ -backfilled DS-MSND could operate in higher temperatures and higher gamma-ray background environments with minimal reduction in neutron detection efficiency.

## 6. Conclusions

The theoretical intrinsic thermal-neutron detection efficiency for DS-MSNDs with straight trenches, circular-holes, and circular pillars of varying dimensions utilizing  $^6\text{LiF}$  or  $^{10}\text{B}$  as neutron conversion material was determined by Monte Carlo simulation with MCNP6.1. The conversion material was considered to have a 50% powder packing fraction based on recently reported results for straight trench DS-MSNDs [17]. All of the DS-MSND geometries show higher efficiency than their single-sided counterparts reported by Shultis and McGregor [11]. The increased performance of DS-MSNDs over MSNDs is attributed to reduction or complete elimination of neutron free-streaming paths through the practically neutron-insensitive semiconductor substrate portions of the microfeatures.

The offset DS-MSND design is simpler to manufacture than the opaque DS-MSNDs, because only one microfeature photolithography mask is required. Also, the etch characteristics of the all microfeatures should be the same, because all the microfeatures are the same dimensions. The offset DS-MSNDs showed the greatest detection efficiency for large feature width to unit cell width ratios. The opaque DS-MSND would be more challenging to manufacture requiring two photomasks and characterization of etching and doping microfeatures of the two sizes. However, high efficiency performance is stretched over a large range of acceptable feature dimensions for a given unit cell width.

For high-efficiency hole and trench patterns, especially in offset DS-MSND designs, the remaining silicon substrate can be very thin, and care must be taken to ensure large dead regions are not formed in the silicon features during the dopant diffusion processes drastically limiting the reaction-product detection sensitivity. In the pillar design, conformal doping of the pillars and adequate backfill into the small surrounding voids could also be challenging.

The detection efficiency was less affected by an increased LLD for DS-MSNDs backfilled with  $^6\text{LiF}$  due to the higher energy reaction products liberated in the  $^6\text{Li}(n, t)\alpha$  reaction. Also, the microfeatures

could be larger for  $^6\text{LiF}$  backfilled DS-MSNDs, because the reaction products have longer ranges in silicon and the conversion material, thereby, allowing for larger (and easier to manufacture) microfeatures.

All designs presented can theoretically achieve intrinsic thermal-neutron detection efficiencies greater than 70%. However, the authors believe the best design is the  $^6\text{LiF}$ -backfilled, straight-trench, offset DS-MSND developed over recent years at Kansas State University because of the manufacturability advantages by utilizing larger feature sizes allowed with  $^6\text{Li}$  absorber, and the microfeature geometry can be achieved through batch-process, anisotropic, wet etching, which reduces costs. The increased diode thickness from 500- $\mu\text{m}$  to 1500- $\mu\text{m}$  required for  $^6\text{LiF}$  is small compared to overall thickness of other types thermal neutron detectors, i.e. gas-filled or scintillation detectors. Future DS-MSNDs devices will be manufactured to improve the neutron sensitivity of previously developed solid-state neutron detector modules like the HeRep, MND, and neutron spectrometer [27–32], as well as other state-of-the-art detector systems where low-profile, power-efficient, high-efficiency neutron detectors are advantageous.

## Declaration of competing interest

The authors declare that they have no known competing financial interests or personal relationships that could have appeared to influence the work reported in this paper.

## Acknowledgment

This work was partially funded by the Defense Threat Reduction Agency (DTRA), Contract number HDTRA1-14-C-0032.

## References

- [1] A. Rose, Sputtered boron films on silicon surface barrier detectors, *Nucl. Instrum. Methods* 52 (1967) 166–170.
- [2] A. Miresghighi, G. Cho, J. Drewery, T. Jing, S.N. Kaplan, V. Perez-Mendez, D. Wildermuth, Amorphous silicon position sensitive neutron detector, *IEEE Trans. Nucl. Sci.* 39 (1992) 635–640.
- [3] S. Pospisil, B. Sopko, E. Havránková, Z. Janout, J. Konicek, I. Mácha, J. Pavlu, Si diode as a small detector of slow neutrons, *Radiat. Prot. Dosim.* 46 (1993) 115–118.
- [4] D.S. McGregor, J.T. Lindsay, C.C. Brannon, R.W. Olsen, Semi-insulating bulk GaAs as a semiconductor thermal-neutron imaging device, *Nucl. Instrum. Methods Phys. Res. A* 380 (1996) 271–275.
- [5] D.S. McGregor, R.T. Klann, H.K. Gersch, Y.H. Yang, Thin-film-coated bulk GaAs detectors for thermal and fast neutron measurements, *Nucl. Instrum. Methods Phys. Res. A* 466 (2001) 126–141.
- [6] D.S. McGregor, M.D. Hammig, Y.-H. Yang, H.K. Gersch, R.T. Klann, Design considerations for thin film coated semiconductor thermal neutron detectors—I: basics regarding alpha particle emitting neutron reactive films, *Nucl. Instrum. Methods Phys. Res. A* 500 (2003) 272–308.
- [7] R.A. Muminov, L.D. Tsvang, High-efficiency semiconductor thermal-neutron detectors, *Sov. At. Energy* 62 (1987) 316–319.

- [8] J. Schelten, M. Balzhäuser, F. Höngesberg, R. Engels, R. Reinartz, A new neutron detector development based on silicon semiconductor and  $6\text{LiF}$  converter, *Physica B: Condens. Matter* 234-236 (1997) 1084–1086.
- [9] D.S. McGregor, R.T. Klann, H.K. Gersch, E. Ariesanti, J.D. Sanders, B. VanDerElzen, New surface morphology for low stress thin-film-coated thermal neutron detectors, *IEEE Trans. Nucl. Sci.* 49 (2002) 1999–2004.
- [10] D.S. McGregor, S.L. Bellinger, J.K. Shultis, Present status of microstructured semiconductor neutron detectors, *J. Cryst. Growth* 379 (2013) 99–110.
- [11] J.K. Shultis, D.S. McGregor, Design and performance considerations for perforated semiconductor thermal-neutron detectors, *Nucl. Instrum. Methods Phys. Res. A* 606 (2009) 608–636.
- [12] S.L. Bellinger, B.W. Cooper, R.G. Fronk, L. Henson, T. Ochs, T.J. Sobering, D.S. McGregor, Characterization of microstructured semiconductor neutron detectors, in: 2013 IEEE Nuclear Science Symposium and Medical Imaging Conference, 2013 NSS/MIC, IEEE, Seoul, South Korea, 2014, pp. 1–7.
- [13] D.S. McGregor, S.L. Bellinger, R.G. Fronk, L. Henson, D. Huddleston, T. Ochs, J.K. Shultis, T.J. Sobering, R.D. Taylor, Development of compact high efficiency microstructured semiconductor neutron detectors, *Radiat. Phys. Chem.* 116 (2015) 32–37.
- [14] T.R. Ochs, S.L. Bellinger, R.G. Fronk, L.C. Henson, C.J. Rietcheck, T.J. Sobering, R.D. Taylor, D.S. McGregor, Fabrication of present-generation microstructured semiconductor neutron detectors, in: 2014 IEEE Nuclear Science Symposium and Medical Imaging Conference, NSS/MIC 2014, IEEE, Seattle, WA, USA, 2016, pp. 1–3.
- [15] S.L. Bellinger, R.G. Fronk, W.J. McNeil, J.K. Shultis, T.J. Sobering, D.S. McGregor, Characteristics of the stacked microstructured solid state neutron detector, in: A. Burger, L.A. Franks, R.B. James (Eds.), in: *SPIE Hard X-ray, Gamma-ray, and Neutron Detector Physics*, Vol. XII, San Diego, CA USA 2010, 78050N.
- [16] S.L. Bellinger, R.G. Fronk, W.J. McNeil, T.J. Sobering, D.S. McGregor, Improved high efficiency stacked microstructured neutron detectors backfilled with nanoparticle  $\text{LiF}$ , *IEEE Trans. Nucl. Sci.* 59 (2012).
- [17] T.R. Ochs, S.L. Bellinger, R.G. Fronk, L.C. Henson, R.M. Hutchins, D.S. McGregor, Improved manufacturing and performance of the dual-sided microstructured semiconductor neutron detector (DS-MSND), *Nucl. Instrum. Methods Phys. Res. A* (2019).
- [18] R.G. Fronk, S.L. Bellinger, L.C. Henson, D.E. Huddleston, T.R. Ochs, C.J. Rietcheck, C.T. Smith, J.K. Shultis, T.J. Sobering, D.S. McGregor, Advancements on dual-sided microstructured semiconductor neutron detectors (DSMSNDs), in: 2015 IEEE Nuclear Science Symposium and Medical Imaging Conference, NSS/MIC, IEEE, San Diego, CA USA, 2016.
- [19] R.G. Fronk, S.L. Bellinger, L.C. Henson, T.R. Ochs, C.T. Smith, J.K. Shultis, D.S. McGregor, Dual-sided microstructured semiconductor neutron detectors (DSMSNDs), *Nucl. Instrum. Methods Phys. Res. A* 804 (2015) 201–206.
- [20] R.G. Fronk, Dual-side etched microstructured semiconductor neutron detectors, in: *Mechanical and Nuclear Engineering*, Kansas State University, 2017.
- [21] R.M. German, *Particle Packing Characteristics*, Metal Powder Industries Federation, Princeton, N.J, 1989.
- [22] D.S. McGregor, J. Kenneth Shultis, Reporting detection efficiency for semiconductor neutron detectors: A need for a standard, *Nucl. Instrum. Methods Phys. Res. A* 632 (2011) 167–174.
- [23] K.-C. Huang, R. Dahal, J.J.-Q. Lu, Y. Danon, I.B. Bhat, High detection efficiency micro-structured solid-state neutron detector with extremely low leakage current fabricated with continuous p-n junction, *Appl. Phys. Lett.* 102 (2013) 152107.
- [24] Y. Danon, J. Clinton, K.C. Huang, N. LiCausi, R. Dahal, J.J.Q. Lu, I. Bhat, Towards high efficiency solid-state thermal and fast neutron detectors, *J. Instrum.* 7 (2012) C03014.
- [25] R.J. Nikolić, A.M. Conway, C.E. Reinhardt, R.T. Graff, T.F. Wang, N. Deo, C.L. Cheung, 6:1 aspect ratio silicon pillar based thermal neutron detector filled with  $\text{B}_{10}$ , *Appl. Phys. Lett.* 93 (2008) 133502.
- [26] R.J. Nikolic, A.M. Conway, C.E. Reinhardt, R.T. Graff, T.F. Wang, N. Deo, C.L. Cheung, Fabrication of Pillar-structured thermal neutron detectors, in: 2007 IEEE Nuclear Science Symposium Conference Record, IEEE, Honolulu, HI, USA, 2007, pp. 1577–1580.
- [27] T.R. Ochs, R.G. Fronk, R.M. Hutchins, D.S. McGregor, D.E. Huddleston, T.J. Sobering, R.D. Taylor, B.L. Beatty, J.A. Gardner, S.L. Bellinger, L.C. Henson, L.M. Whitmore, Wearable neutron detector for dosimetry and nuclear non-proliferation, in: *International Conference on the Security of Radioactive Material: The Way Forward for Prevention and Detection*, Vienna, Austria, 2018.
- [28] T.R. Ochs, S.L. Bellinger, R.G. Fronk, L.C. Henson, D.E. Huddleston, G.E. Schlaikier, T.J. Sobering, A. Van Bergeijk, D.S. McGregor, Fourth-generation microstructured semiconductor neutron detector (MSND)-based  $^3\text{He}$  replacement (HeRep) for high pressure  $^3\text{He}$  detectors, in: 2016 IEEE Nuclear Science Symposium, Medical Imaging Conference and Room-Temperature Semiconductor Detector Workshop, NSS/MIC/RTSD, IEEE, Strasbourg, France, 2017, pp. 1–5.
- [29] R.G. Fronk, S.L. Bellinger, L.C. Henson, D.E. Huddleston, T.R. Ochs, T.J. Sobering, D.S. McGregor, High-efficiency microstructured semiconductor neutron detectors for direct  $^3\text{He}$  replacement, *Nucl. Instrum. Methods Phys. Res. A* 779 (2015) 25–32.
- [30] T.R. Ochs, B.L. Beatty, S.L. Bellinger, R.G. Fronk, J.A. Gardner, L.C. Henson, D.E. Huddleston, R.M. Hutchins, T.J. Sobering, J.L. Thompson, A. Van Bergeijk, D.S. McGregor, Wearable detector device utilizing microstructured semiconductor neutron detector technology, *Radiat. Phys. Chem.* 155 (2019) 164–172.
- [31] C.B. Hoshor, E.R. Myers, T.M. Oakes, S.M. Young, J.E. Currie, P.R. Scott, W.H. Miller, S.L. Bellinger, D.S. McGregor, A.N. Caruso, Real-time neutron source localization and identification with a hand-held, volumetrically-sensitive, moderating-type neutron spectrometer, *Nucl. Instrum. Methods Phys. Res. A* 866 (2017) 252–264.
- [32] C.B. Hoshor, T.M. Oakes, E.R. Myers, B.J. Rogers, J.E. Currie, S.M. Young, J.A. Crow, P.R. Scott, W.H. Miller, S.L. Bellinger, T.J. Sobering, R.G. Fronk, J.K. Shultis, D.S. McGregor, A.N. Caruso, A portable and wide energy range semiconductor-based neutron spectrometer, *Nucl. Instrum. Methods Phys. Res. A* 803 (2015) 68–81.